



university of
 groningen

Diffusive Shock Acceleration with CR Propa

by

Aritra Ghosh

Primary Supervisor:

Prof. Olaf Scholten

A thesis submitted in partial fulfillment for the degree of
 Master of Science

in the
 Faculty of Science & Engineering
 Program: Physics (Quantum Universe Track)

June 2017

Supervisor & First Examiner:- Prof. Olaf Scholten

Second Examiner:- Prof. A. M. van den Berg

This work was done in collaboration with the Astronomy & Astrophysics group at Vrije universiteit Brussel (VuB) and contains a considerable amount of input from Prof. Stijn Buitink and Dr. Tobias Winchen.

The code used and developed within the course of this work will be published online within the CR Propa examples on the CR Propa website (www.crpropa.desy.de).

A portion of this work will appear in *Proceedings of Science* as a part of the proceedings of the 35th International Cosmic Ray Conference.

I have been financially supported during the time of this work by the Maria Sibylla Merian Scholarship of the Faculty of Science & Engineering, an Erasmus+ grant from the Erasmus Programme and a masters grant from the Groningen University Fund.

“Rome ne fut pas faite toute en un jour”
(Rome wasn't built in a day)

- medieval French phrase from the collection *Li Proverbe au Vilain*

UNIVERSITY OF GRONINGEN

Abstract

Faculty of Science & Engineering
Program: Physics (Quantum Universe Track)

Master of Science

by [Aritra Ghosh](#)

CR Propa is a public astrophysical simulation framework for studying propagation and interaction physics of primary and secondary cosmic ray particles. We have incorporated particle acceleration within CR Propa and run a series of consistency tests to regenerate classic cases such as that of Diffusive Shock Acceleration or first order Fermi Acceleration. This has enabled us to investigate the nuances of acceleration-region geometry, the process of particle acceleration, the role of scattering centres and verify various theoretical predictions as well to a great detail. In future, this development will allow incorporation of various loss mechanisms, production of secondaries within the simulation model quite easily due to pre-existing capabilities of CR Propa.

Acknowledgements

I have worked on this thesis for almost the entirety of the past year and it wouldn't have been such a fruitful and enjoyable experience without the help of so many people.

I am particularly grateful to my supervisor, Prof. Olaf Scholten for all the help and support he has provided during this period. His sharp insight about cosmic rays, particle acceleration and different matters of scientific research in general has come in extremely handy. He has at times nudged me in the correct direction while giving me at all instances a lot of freedom regarding which direction this project should be taken. Besides professional advice, I have also had the opportunity to dwell on personal matters with him and I have come to value his opinion greatly.

During the course of this work, I spent around three months at Vrije Universiteit Brussel in early 2017 and the time I spent there proved to be extremely fruitful. Prof. Stijn Buitink's and Dr. Tobias Winchen's expertise on shock acceleration and CR Propa meant that during every step of the way, I had someone to turn into when I ran into problems. Besides, Tobias' tips about different aspects of writing a thesis also came in handy during the preparation of this document. Lastly, all the blackboard/lunch/coffee-room discussions also involving Pragati Mitra and Dr. Katharine Mulrey contributed a lot to my general understanding of the "scientific" process of research besides producing some great inputs for this project.

As always, I am eternally grateful to my family back home in Kolkata for all their love and support. It's their enthusiasm, motivation and care which have helped me to tide over the most difficult parts of my last two years in Groningen. I shall always revere them for the values and the love for knowledge/education that they have instilled in me.

I am particularly grateful for the good times and assistance given by many people in Groningen like Tamalika di, Arijit da, Caelan, Joe, Manvi, Susan, Cristina and many others. They kept my spirits up and made sure I had a family even when I was away from home. To Preetha, Satyanu, Souradeep, Sharbatanu, Soham and the rest – thank you for all your help and those innumerable text and video chats. You guys have shown that distance hardly matters when it comes to friends and significant others.

Lastly, I would also like to acknowledge the help I have received from my professors and the administrative staff of different units of the university such as the KVI, the Masters Physics Program and the International Office of the FSE.

—Aritra

June 28, 2017

Contents

Abstract	iii
Acknowledgements	iv
Abbreviations & Units	vii
1 Introduction	1
1.1 Cosmic Rays and CR Propa	1
1.2 Cosmic Ray Sources and Particle Acceleration	3
1.3 Diffusive Shock Acceleration	4
1.4 Structure of the Thesis	6
2 Diffusive Shock Acceleration Theory	7
2.1 Particle Dynamics in a Magnetic Field	7
2.2 Motion of High Energy Particles in a Plasma	9
2.3 Basics of Shock Waves	11
2.4 Physics of DSA	13
3 Simulation of DSA	19
3.1 CR Propa	19
3.2 Simulation Setup	21
3.2.1 Geometry	21
3.2.2 Methodology	23
3.2.3 Modification of the Scattering Rate	24
3.3 Calibration & Initial Checks	25
4 Results	29
4.1 Downstream Box Size	29
4.2 Relative Energy Gain & Return Probability	33
4.3 Mean Free Path	36
4.4 Energy Dependent Scattering Rate	37
4.5 Variable Scatter Centre Density	39
4.6 Application to Experimental Results	42
5 Conclusion	45

A Spectrum Images

47

Bibliography

54

Abbreviations & Units

CR	Cosmic R ay
UHECR	Ultra H igh E nergy CR
SNR	Supernova R emnant
AGN	Active G alactic N uclei
GRB	G amma R ay B urst
DSA	Diffusive S hock A cceleration
MHD	Magneto H ydrodynamic(s)
MFP	Mean F ree P ath

EeV	10^{18} eV
PeV	10^{15} eV
TeV	10^{12} eV
pc	3.0857×10^{16} m

Chapter 1

Introduction

1.1 Cosmic Rays and CR Propa

Cosmic rays (CRs), which are highly energetic particles incessantly bombarding the Earth's atmosphere, were the first hint that there is much more to this universe than simply stars, gas and dust. Since their discovery in the early 1900s, cosmic rays have become well known and served as an important source of knowledge to the physics community.

Over the last few decades, multiple aspects of cosmic rays have been investigated thoroughly through various experiments, with the most notable feature being the steeply falling energy spectrum with a cut-off above ~ 40 EeV ($1 \text{ EeV} = 10^{18} \text{ eV}$) [1]. Fig. 1.1, which has been reproduced from Ref. [2], shows the cosmic ray spectrum by combining data from various experiments. Barring a few exceptions, cosmic ray arrival directions have remained more or less isotropic [2] and detailed analysis of cosmic ray induced air showers have revealed a composition with contribution of large nuclear masses above ~ 4 EeV [3]. It should be mentioned here that it is still very unclear how large the contribution of heavy nuclei really is. Auger and Telescope Array [4] seem to point in different directions even though their results are consistent within systematic uncertainties.

In spite of what we have come to know about cosmic rays over the course of the last century, they have managed to remain abstruse with respect to many aspects. Especially the observation of ultra high energy cosmic rays (UHECRs) with energies above 10^{20} eV have posed some interesting questions with regards to their origin, acceleration mechanisms, distribution and nature of their sources, the nature of the particles, interaction mechanisms etc. and none of these questions have been completely answered till date.

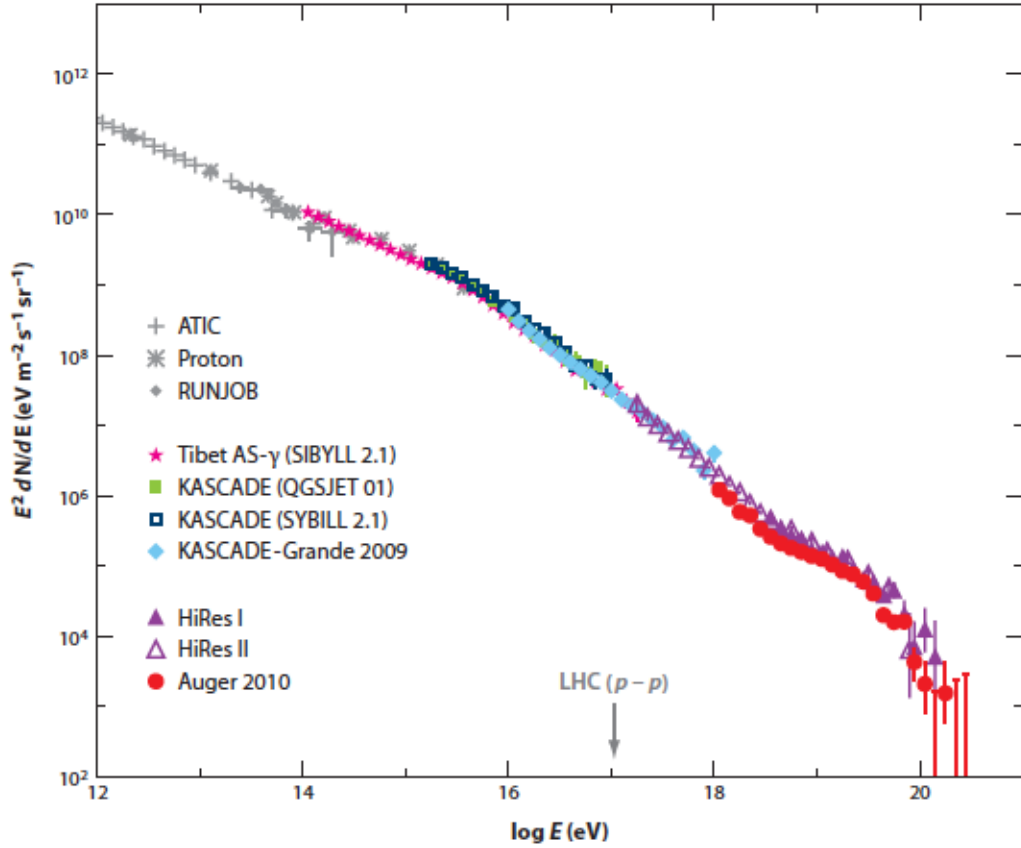


FIGURE 1.1: All particle cosmic ray flux multiplied by E^2 observed by ATIC (Advanced Thin Ionization Calorimeter), Proton, RUNJOB (Russian Nippon Joint Balloon experiment), Tibet AS- γ (Tibet Air-Shower Gamma Experiment), KASCADE (Karlsruhe Shower Core and Array Detector), KASCADE-Grande, HiRes I (High Resolution Fly’s Eye I), HiRes II and Auger (the Pierre Auger Observatory). Large Hadron Collider (LHC) energy reach of p-p collisions (in the frame of a proton) is indicated for comparison. Reproduced from Ref. [2]

In their efforts to further knowledge with respect to cosmic rays, physicists regularly need to reconcile experimental data with current knowledge about large-scale structures, magnetic fields, nuclear decay, particle interaction with background fields and other related physics. Only when so many different aspects are taken into account does a coherent picture emerge. Knowledge in many of these aspects have expanded quite significantly in the last few decades and a single numerical tool that combines all this knowledge is extremely useful. This tool can then be used to invalidate multiple theoretical scenarios and make progress towards an astrophysical model that can account for all measurements simultaneously.

CR Propa 3 [5] is such a publicly available simulation tool that simulates different astrophysical scenarios and produces as output primary and secondary cosmic ray particles such as protons, pions, nuclei, charged leptons, neutrinos and photons. CR Propa 3 has a modular structure with the names of the different modules being self explanatory:-

Source Module, Propagation Module, Interaction Module etc. Given an input of certain particle(s), CR Propa makes each of these modules operate on each of these particles and follows their characteristics throughout the simulation. The availability of such modules enables users to construct and investigate an astrophysical scenario according to their wishes.

CR Propa 3 also allows users to define their own modules to extend the astrophysical scenarios. This thesis primarily focuses on the incorporation of a Diffusive Shock Acceleration (DSA) module within CR Propa. DSA and the motivation behind incorporating it within CR Propa are discussed in Sec. 1.3

1.2 Cosmic Ray Sources and Particle Acceleration

Physicists have always been fascinated by the question about the origin of CRs. Although we now have some basic ideas about possible sources, the issue is far from being settled definitively. Besides, the last few years have especially seen an uptick in observations, theoretical progress and genuine interest in the topic particularly due to its relevance in the indirect detection of dark matter.

The best starting point to talk about CR sources is the CR spectrum. As is evident from Fig. 1.1, the CR spectrum is not free from specific features – the “knee” at around 10^{15} eV and the “ankle” in the range of $10^{18} - 10^{20}$ eV are well-known features. However, in spite of these features, the overall spectrum retains a power law form over the entire fifteen decades from MeV to ZeV. This uniformity strongly suggests that similar processes are responsible for the acceleration of all these particles and it is widely believed that these acceleration mechanisms are connected to different kinds of shocks [6]. The lowest energy particles are believed to derive their energy from shocks in the planetary magnetosphere, interplanetary space and the sun. Shocks related to galactic supernova remnants (SNRs) are thought to be the primary accelerators for particles up to the knee [7] – the knee itself occurs presumably because this is the highest energy that particles can be accelerated to by galactic SNRs. Simple considerations about the confinement of particles in the galaxy and the galactic halo require that UHECRs (i.e. the particles beyond the ankle) be primarily of extragalactic origin [8] and the various candidates for their acceleration are Active Galactic Nuclei (AGN) [9], Gamma Ray Bursts (GRBs) [10], spinning magnetars [11] and intergalactic shock fronts [12]. Thus the transition from galactic to extragalactic CRs occurs somewhere between the knee and the ankle, but there is no agreement on the exact location of this transition. In this region, shocks which are larger than those associated with individual SNRs, such as supershells and a galactic wind termination shock are suggested sources [7].

As demonstrated in the last paragraph, particle acceleration is intertwined with any discussion about CR sources. Therefore, any discussion on CR sources require a detailed and robust understanding of the acceleration process therein and hence the interest in this domain.

1.3 Diffusive Shock Acceleration

Diffusive Shock Acceleration (DSA) was first proposed in the late 1970s independently by multiple groups [13, 14] in the context of acceleration of galactic CRs. It is widely believed to be the primary mechanism by which the Sedov-Taylor blast waves of SNRs accelerate galactic CRs up to the knee of the CR spectrum. Being the primary mechanism for charged particles to gain non-thermal energy near strong shock waves, DSA has dominated much of astrophysical thinking since the 1970s in the domain of particle acceleration.

DSA primarily relies on the repeated scatterings of charged particles by magnetic irregularities (Alfvén waves) frozen inside a magnetic plasma near a shock-front. The most notable and well-known feature of this acceleration process is probably the fact that it results in a power law spectrum with a spectral index close to -2.0 (for the standard case of non-relativistic strong shocks). The power law results from the combination of the energy gain in each shock crossing and the probability of the particle to escape from the acceleration region after each such acceleration cycle. Thus, it is a modified realisation of the statistical acceleration process proposed by Fermi in 1949 [15] and hence it is also known by the name “first order Fermi acceleration”.

A power law with a spectral index of -2.0 happens to be extremely exciting for any source acceleration process because it is not far from what is required for a theory of galactic cosmic rays. The observed spectrum of these particles is $N(E)_{obs} dE \propto E^{-2.7}$ (the region below the “knee” in the CR spectrum shown in Fig. 1.1) and this can be explained by a source spectrum $N(E)_s dE \propto E^{-s}$ with s in the range $2.1 \lesssim s \lesssim 2.4$ combined with energy dependent propagation effects [16]. Besides, for synchrotron emission from non-thermal radio sources such as supernova remnants and lobes of radio galaxies, the spectrum of the GeV electrons responsible are similar to the one described above with the power law slope in the range $s \sim 2.1 - 2.7$ [16]. It should be mentioned here that while there are various mechanisms (such as energy losses) which can make the spectrum softer, it is in general more difficult to produce a harder spectrum with DSA.

Most of what we know about CR sources and the acceleration mechanisms derive from astronomical observations across the electromagnetic spectrum and the above paragraphs are no exception. The Chandra X-Ray observatory has nearly matched the resolution of radio maps of SNRs and showed signs of electron synchrotron emission from the bounding shock fronts [7](See Fig. 1.2). It has also provided strong evidence that high Mach number shocks can accelerate CR electrons up to ~ 100 TeV [17]. Direct evidence for proton acceleration in this domain has been rather recent from the Fermi and AGILE observations [18, 19].

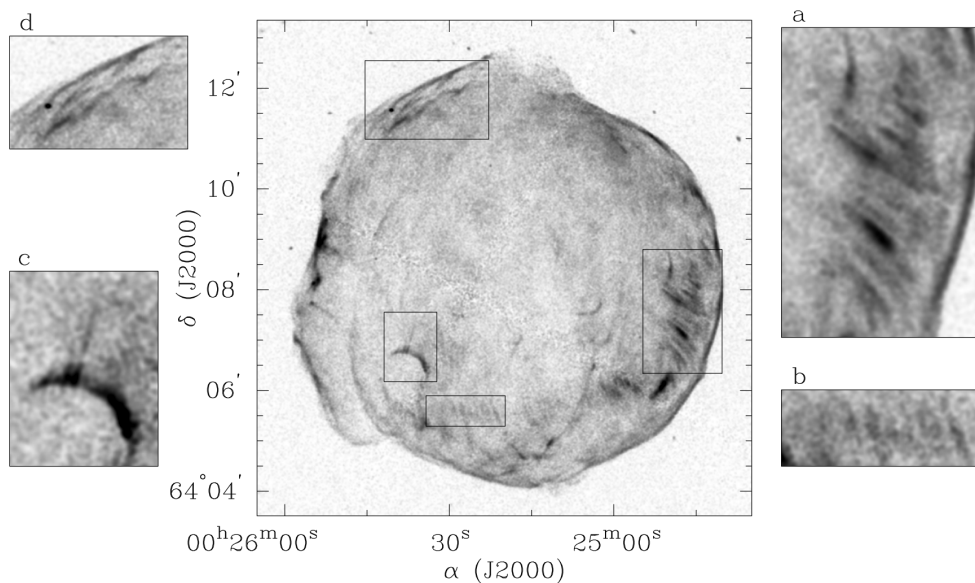


FIGURE 1.2: Chandra X-ray 4.0 - 6.0 keV image of the Tycho supernova remnant, showing detailed non-thermal emitting features manifesting the shock fronts. Reproduced from Ref. [17]

Recent developments in astroparticle physics have also resulted in modified versions of DSA being used to explain scenarios beyond its “traditional” domain. In recent years, the Ice Cube Collaboration has reported the existence of high energy extraterrestrial neutrinos [20]. These PeV regime neutrinos have generated a lot of interest as they may provide valuable information on hadronic acceleration sites. However, till now, no significant correlations have been observed with matter distributions [20] or cosmic ray arrival directions [21] and the astrophysics community has been rife with speculation about their sources. One of the claims has been that some of these neutrinos could have their roots in star-burst regions with multiple powerful winds of young massive stars and SNRs [22]. The authors argue that a SN shock colliding with a fast wind arising from a young cluster of stars can accelerate protons to energies well above the standard upper limits of DSA and argue that SN shocks in the Westerlund 1 cluster in the Milky Way may accelerate protons to $\gtrsim 40$ PeV [22]. Once accelerated, these CRs can then diffuse

into the surrounding medium and produce a neutrino flux, consistent with a fraction of the Ice Cube observations.

Thus, DSA has played a historically important role with respect to acceleration of CRs and continues to be relevant even today. Now, the question arises as to what benefits does it entail to incorporate DSA within CR Propa. Numerical studies of DSA are nothing new – they were started as early as the 1980s [23], just a few years after their theoretical introduction – and they continue even today with recent studies employing particle-in-cell (PIC) approaches [24]. While the focus of the community has been on macroscopic studies, observing how the properties of the plasma evolve with time, there has been almost no significant effort to follow the process microscopically (i.e. following the properties of each particle individually) and justifiably so, due to the long computational times involved and the little additional benefits it brings with itself. However, development of computational power over the last decade and a numerical tool like CR Propa completely change this scenario. If DSA is successfully incorporated within CR Propa, then this opens the door to many new potential results as this allows us to venture into uncharted territory like what happens when we combine DSA with various loss mechanisms, interaction with background fields, production of secondaries. Since modules that deal with various particle interactions, decays etc. are already present within CR Propa, once a new module dealing with DSA is introduced, these new scenarios can be studied quite easily by combining these various modules. Understanding how the various parameters of the microscopic simulation are related to the analytical results is the first step towards these more complicated scenarios.

1.4 Structure of the Thesis

This thesis will primarily deal with the incorporation of a new module dealing with DSA into CR Propa. To prove the robustness of the tool, some classic results will be reproduced while some new situations will be studied by tweaking these classic scenarios. This Chapter has given a basic idea of DSA and laid out the motivation behind this work. Chapter 2 will deal with the theory of DSA in detail. In Chapter 3, technical details of CR Propa and the simulation setup will be discussed along with some initial consistency and calibration tests performed on it. Chapter 4 will contain all the results that have been generated by the newly incorporated module and finally, Chapter 5 will contain a concluding summary and a discussion about future applications of this work.

Chapter 2

Diffusive Shock Acceleration Theory

This chapter will lay out the theory behind DSA in substantial detail, to the extent necessary for understanding the later parts of this thesis. Diffusive Shock Acceleration happens to be a completely non-dynamical acceleration process i.e. the mechanism is completely collisionless – the particles do not gain any energy via collisions. There are two parts to this process – the particles get scattered by magnetic irregularities frozen in the plasma and they cross shock fronts. A combination of these two mechanisms lead to the acceleration as will be elucidated below. First, Secs. 2.1, 2.2 will focus on particle dynamics in a plasma and shock waves in general – then using this background information the actual mechanism will be laid out in Sec. 2.4. Any analytical discussion on DSA can proceed via two routes: a) the macroscopic one, where starting with the Fokker-Planck equation, one follows the momentum distribution of particles in the vicinity of the shock b) the microscopic one, wherein the behaviour of individual particles are followed. Since our simulation is a microscopic one, we proceed via the second route. All the content in Sec. 2.1 - 2.4 will be based on the arguments of Ref. [13, 25] and Chapters 7,11,17 of Ref. [26]

2.1 Particle Dynamics in a Magnetic Field

Magnetic fields are present everywhere in astrophysical environments and hence the Lorentz Force $\vec{F} = q(\vec{v} \times \vec{B})$ governs particle dynamics in astrophysical scenarios.

Let us start with the simple case of a uniform static magnetic field. It is well known that in this scenario, the motion of the particle is helical around the magnetic field line(s) –

the particle keeps gyrating in a circular path about its “guiding centre” and this guiding centre translates along the magnetic field lines with a constant velocity. This motion is shown in Fig. 2.1

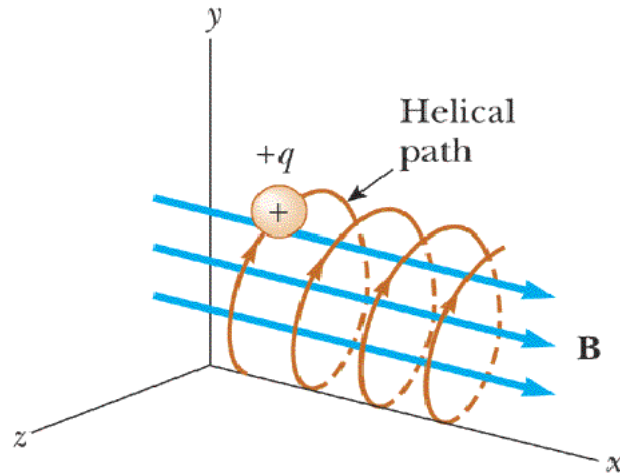


FIGURE 2.1: The motion of a charged particle in a static uniform \vec{B} field. The guiding centre moves parallel to the blue lines. Image from titan.bloomfield.edu

However, in real life, magnetic fields are rarely static and uniform – the magnetic field distribution can vary both with time and spatial position. Let us consider the case where the magnetic field \vec{B} varies slowly with time, by which we mean that the fractional change in the strength of the magnetic field $\frac{\Delta B}{B}$ changes very little during one orbital period of the particle around the field lines. In this case as well, the motion of the particle is best visualised in terms of the “guiding centre” picture. It can be shown from simple electromagnetic arguments (see Ref. [26] for details) that the particle’s motion is such that $\Delta(Br^2) = 0$ where r is the gyro-radius of the particle. Therefore, the particle follows its guiding centre in such a way that the number of magnetic field lines within the particle’s orbit always remains constant as shown in Fig. 2.2.

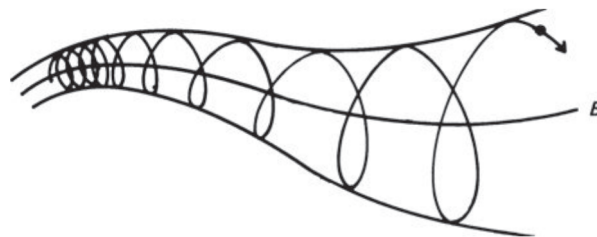


FIGURE 2.2: Dynamics of a charged particle in a slowly varying magnetic field. The particle always encloses a constant number of field lines. Reproduced from Ref. [26]

According to the arguments in the last paragraph, charged particles move in such a way that they enclose the same field lines as long as the field is slowly varying. However,

there are bound to be situations in real life, where a magnetic field will have abrupt irregularities. The dynamics of the particles then depend on the scale of the fluctuations in the magnetic field ΔB compared to the gyro-radii r of the particles. If $r \ll \Delta B$, then the particle trajectories follow their guiding centre and the pitch angle changes according to the invariant described in the last paragraph i.e. the motion is as shown in Fig. 2.2. In the other extreme, $r \gg \Delta B$, the particles, in a sense, do not “see” these tiny fluctuations at all and their overall motion is governed by the mean magnetic field which is much larger than the fluctuations. This is shown in Fig. 2.3 (a). In the scenario where $r \approx \Delta B$, the particles undergo a significant amount of scattering in their pitch angle as shown in Fig. 2.3 (b). If the magnetic field irregularities are random, then the scatterings will also be random and this will result in a uniform distribution of pitch angles.

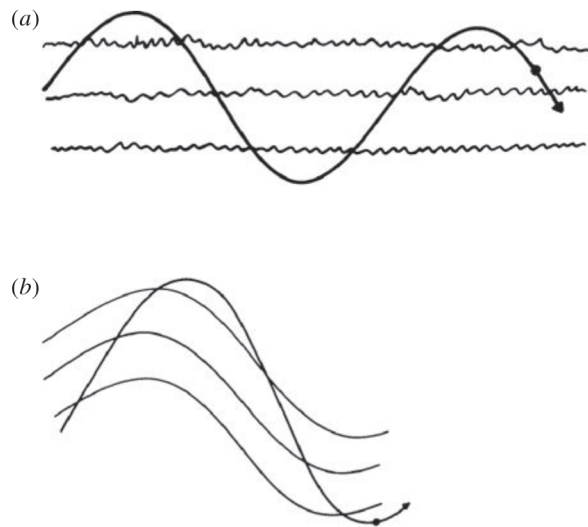


FIGURE 2.3: Motion of a charged particle when (a) the irregularities in the magnetic field are on a much smaller scale than the particle’s gyroradius (b) when they are of the same order of magnitude. Reproduced from Ref. [26]

2.2 Motion of High Energy Particles in a Plasma

This section will deal with what happens when there is a magnetic field embedded inside a plasma and a flux of high energy particles propagate at a high streaming velocity along the magnetic field direction. Just like any other gas, acoustic and electromagnetic waves can propagate through a plasma. However, in addition, due to the fact that they are ionised, plasmas can also sustain electrostatic and magneto-hydrodynamic (MHD) Alfvén waves. Because a plasma happens to be inherently non-linear, dissipative and dispersive, the general theory of plasma waves is quite complicated and outside the scope of this thesis. However, for our purposes, the Alfvén wave can be considered as a low frequency wave in a plasma consisting of travelling oscillations of the ions and

the magnetic field. The ion mass provides the inertia and the magnetic field tension provides the restoring force. The phase velocity of these Alfvén waves is referred to as the Alfvén velocity.

Now, if the plasma happens to be fully ionised, then the high energy particles resonate with the irregularities in the embedded magnetic field and get scattered in pitch angle exactly as described in Sec. 2.1. Besides, the streaming motion also amplifies the MHD Alfvén waves which in turn generates magnetic fluctuations – therefore, even if there were no magnetic irregularities to begin with, the streaming motion of the particles itself gives rise to the irregularities and then these particles themselves get scattered due to these irregularities. Physically speaking, the energy in the forward motion of the beam of particles is transferred to the waves, which must grow as a result and this instability keeps on developing until the streaming velocity of the high energy particles is reduced by scattering to the Alfvén velocity. This mechanism, therefore, prevents the streaming of cosmic rays along the magnetic field lines and at the same time isotropizes the particle distribution in pitch angle. For a more involved and detailed discussion please refer to the following reviews [27, 28].

The considerations of the above two paragraphs lead to the result that because of random scattering by irregularities in the magnetic field, either associated with fluctuations in the field or with growing Alfvén waves caused by the streaming motion of the particles, high energy charged particles can always be considered to be “effectively” performing diffusion in a plasma. As the particles diffuse in a plasma they may also be subject to energy gains and losses. A very helpful tool to study such a process is the diffusion-loss equation which describes the energy spectrum of the particles as they diffuse in the plasma. The equation is derived in the following paragraph.

Let us assume a volume dV in which particles are subject to energy gains and losses, given by

$$-\frac{dE}{dt} = b(E)$$

where if $b(E)$ is positive the particles lose energy. At a time t , the number of particles in the energy range E to $E + \Delta E$ is $N(E)\Delta E$. At a later time, $t + \Delta t$, these particles are replaced by those that had energies in the range E' to $E' + \Delta E'$ at time t , where

$$E' = E + b(E)\Delta t$$

and

$$E' + \Delta E' = (E + \Delta E) + b(E + \Delta E)\Delta t.$$

Performing a Taylor expansion for small values of ΔE and subtracting, we have

$$\Delta E' = \Delta E + \frac{db(E)}{dE} \Delta E \Delta t.$$

Therefore, the change in $N(E)\Delta E$ in the time interval Δt is

$$\Delta N(E)\Delta E = -N(E, t)\Delta E + N(E + b(E)\Delta t, t)\Delta E'.$$

Performing another Taylor expansion for small $b(E)\Delta t$ and substituting for $\Delta E'$, we obtain

$$\Delta N(E)\Delta E = \frac{dN(E)}{dE} b(E)\Delta E \Delta t + N(E) \frac{db(E)}{dE} \Delta E \Delta t$$

that is

$$\frac{dN(E)}{dt} = \frac{d}{dE} [b(E)N(E)]. \quad (2.1)$$

This equation represents the particle spectrum in the volume dV subject only to energy gains and losses. If particles are injected into this volume at a rate $Q(E, t)$ per unit volume, then the equation becomes

$$\frac{dN(E)}{dt} = \frac{d}{dE} [b(E)N(E)] + Q(E, t). \quad (2.2)$$

Particles also enter and leave this volume by diffusion and this process depends upon the gradient of the particle density $N(E)$. Assuming a scalar diffusion coefficient, the final form of the diffusion loss equation is given by

$$\frac{dN(E)}{dt} = \frac{d}{dE} [b(E)N(E)] + Q(E, t) + D\nabla^2 N(E). \quad (2.3)$$

2.3 Basics of Shock Waves

Perturbations in a gas are propagated away at the speed of sound. Now, if there is a disturbance in the gas propagating at a velocity greater than the speed of sound, then there arises a discontinuity in between the regions ahead and behind the disturbance, the former region having no prior ‘‘information’’ about the imminent arrival of the disturbance. These discontinuities are called shock waves. They are quite ubiquitous in high energy astrophysics and are of course at the heart of DSA as the name suggests.

Let there be a shock wave propagating through a stationary medium with a supersonic velocity U as shown in Fig. 2.4(a). The physical properties of the gas vary on both sides of the shock as depicted in the figure. In most cases, while analysing shocks it is almost standard to do it from the rest frame of the shock front. If we transform to the rest frame of the shock front, then the situation is as depicted in Fig. 2.4(b). The

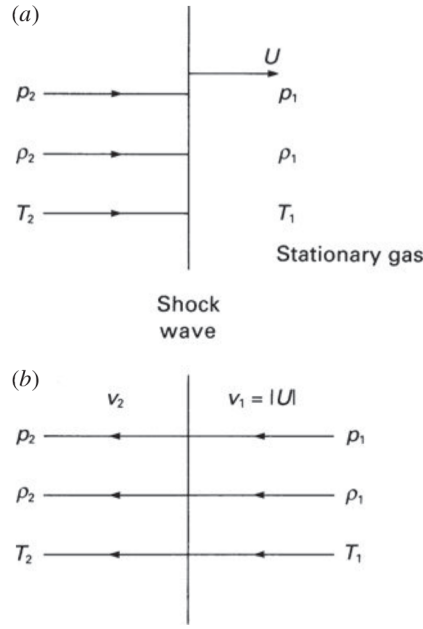


FIGURE 2.4: (a) A shock wave propagating through a stationary gas at a supersonic velocity U . (b) The same situation visualised in the rest frame of the shock front. Reproduced from Ref. [26]

gas in front of the shock (upstream gas) now travels towards the shock with a velocity which is of the same magnitude as U . After the gas passes through, it moves away from the shock (downstream gas) with a different velocity. Now, to relate the parameters on both sides of the shock, we conserve the mass, energy flow and momentum flow across the shock front. Assuming a perfect gas with a ratio of specific heat capacities γ_C , the following three relations arise in the limit $M_1 \gg 1$ where M_1 is the Mach number of the shock wave.

$$\frac{p_2}{p_1} = \frac{2\gamma_C M_1^2}{(\gamma_C + 1)} \quad (2.4)$$

$$\frac{\rho_2}{\rho_1} = \frac{\gamma_C + 1}{\gamma_C - 1} \quad (2.5)$$

$$\frac{v_2}{v_1} = \frac{\gamma_C - 1}{\gamma_C + 1} \quad (2.6)$$

$$\frac{T_2}{T_1} = \frac{2\gamma_C(\gamma_C - 1)M_1^2}{(\gamma_C + 1)^2} \quad (2.7)$$

where p, ρ, T, v are as defined in Fig. 2.4. Therefore, as the undisturbed gas passes through the shock, it is both heated and accelerated by it (in the “lab” frame). Note that while v_2/v_1 and ρ_2/ρ_1 are fixed for a particular γ_C , T_2/T_1 and p_2/p_1 scale with M_1 .

Thus, although we can reach a compression factor of only 4 even with a strong shock (for $\gamma_C = 5/3$), we can get extremely efficient heating for such shocks.

2.4 Physics of DSA

Now, let us finally come to DSA. The model involves a strong shock propagating through a diffuse medium (with a velocity U as shown in Fig. 2.5 (a)) for eg. the shock waves which propagate through the interstellar medium ahead of supersonic shells of supernova remnants. High energy particles are assumed to be present both in the upstream and downstream regions and they are assumed to be propagating close to the speed of light i.e. the velocity of the shock is much less compared to that of the particles.

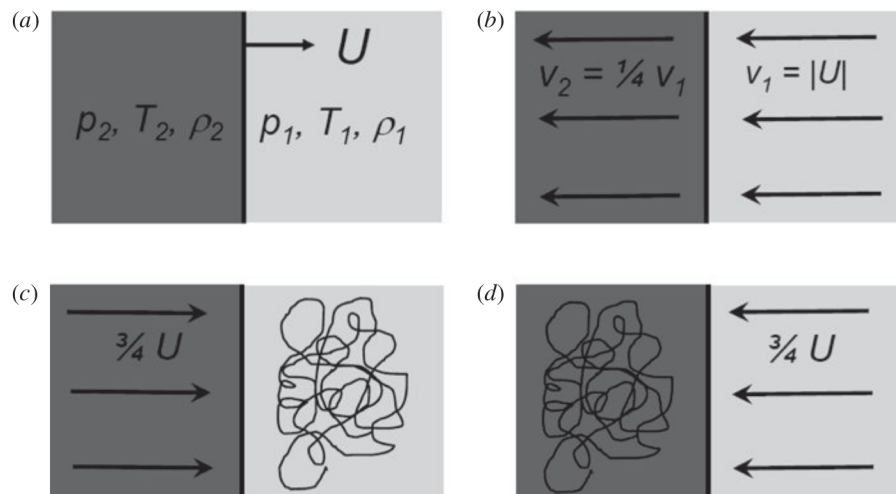


FIGURE 2.5: (a) A strong shock propagating through stationary interstellar gas at velocity U . The parameters of the upstream and downstream regions are also shown. (b) The situation from the rest frame of the shock. (c) The situation from the rest frame of the upstream gas (d) The situation from the rest frame of the downstream gas. Reproduced from Ref. [26]

Now, due to reasons described in Sec. 2.2, as the high energy particles try to stream through the upstream and downstream regions, they are scattered by magnetic irregularities and plasma instabilities. As these scatterings happen to be random, the velocity distribution of the particles rapidly becomes isotropic in the reference frame of the moving fluid on either side of the shock. Therefore, the operating mechanism of DSA entails high energy particles gaining energy in shock crossings (as will be demonstrated below) and then their velocity distribution becoming isotropic due to scatterings in the plasma. Finally, depending on the probability of escape from the acceleration region, they either cross the shock front again and repeat the same cycle or exit the acceleration region.

Thus, at each shock crossing, the particle keeps gaining energy and the escape probability determines the number of such crossings a particle undergoes. It is important to emphasise that the particle's energy is conserved in the rest frame of the plasma during the scattering process and it gains energy only during shock crossings. It should be noted that this energy gain does not happen magically “at” the shock-front. It is the process of crossing the shock and isotropization thereafter which causes the gain.

We reviewed the basics of strong shock waves in Sec. 2.3. Now, the material ejected in supernova explosions attains a velocity of the order of 10^4 km s^{-1} which is much greater than the Alfvén speeds of the interstellar medium (which are at the most 10 km s^{-1}) and hence we can apply the theory of strong shocks here. Just like there, here also, for the ease of analysis, we move into the rest frame of the shock as shown in Fig. 2.5 (b). In this frame, the upstream gas is now moving into the shock with a velocity $v_1 = U$ and the downstream gas is moving away with a velocity v_2 . Taking $\gamma_C = 5/3$ for a mono-atomic or fully ionised gas and plugging it into Eq. 2.6, we get $v_2 = (1/4)v_1$ just as was shown in Fig. 2.5 (b).

For fully understanding the process, let us now analyse (c) and (d) of Fig. 2.5. Let us consider Fig. 2.5 (c) first. This is the rest frame of the upstream gas – scattering ensures that the upstream particle distribution is isotropic in this frame. Here, the shock is moving at a velocity U , but the downstream gas is now moving towards the shock at a velocity $(3/4)U$. After an upstream particle crosses the shock-front, it obtains a small increase in energy, of the order $\Delta E/E \sim U/c$ (as will be shown below). The particles are then scattered in the region behind the shock so that their velocity distributions become isotropic with respect to that flow.

For the opposite scenario of a particle diffusing from the downstream to the upstream region, refer to the rest frame of the downstream gas (Fig. 2.5 (d)). Here, the velocity distribution of particles is isotropic behind the shock and when the particles cross the shock front, they encounter gas moving towards the shock front with the same velocity $(3/4)U$. Thus, the same series of processes repeats itself, by which the particle gains a small amount of energy and scatters thereafter. This is one of the notable features of this acceleration mechanism – there are no shock crossings in which the particle loses energy. It always gains energy (as long as the situation is analysed from the frames described above) unlike the original mechanism proposed by Fermi. (second order Fermi acceleration [15]).

Now let us get into the mathematics of this process. Let the time-rate of energy increase of the particle be given by

$$\frac{dE}{dt} = \alpha E$$

and let the particle remain in the acceleration region for a time τ_{esc} . To find out the resulting spectrum we employ the diffusion-loss equation (Eq. 2.3). We are interested in the steady state solution in the absence of diffusion and so $\frac{dN}{dt} = 0$ and $D\nabla^2 N = 0$. We also assume that there are no sources and hence $Q(E) = 0$. The energy loss term $b(E) = -\frac{dE}{dt}$ now becomes an energy gain term $b(E) = -\alpha E$. Therefore Eq. 2.3 now becomes

$$-\frac{d}{dE} [\alpha E N(E)] - \frac{N(E)}{\tau_{esc}} = 0. \quad (2.8)$$

Differentiating and rearranging this equation,

$$\frac{dN(E)}{dE} = - \left(1 + \frac{1}{\alpha \tau_{esc}} \right) \frac{N(E)}{E}$$

and so

$$N(E) = constant \times E^{-x} \quad (2.9)$$

where $x = 1 + (\alpha \tau_{esc})^{-1}$. Therefore, this mechanism of gaining energy stochastically and a finite probability of escape (that is the basic original Fermi mechanism) itself guarantees a power law. Now, let us see how we arrive at a specific value of $x = 2$ for DSA.

First of all, let us rewrite the essence of the original Fermi mechanism in a slightly different way. We define two constants β and P as follows: $E = \beta E_0$ is the average energy of the particle after one shock crossing and P is the probability that the particle remains within the acceleration region after one crossing. Then, after k crossings, there are $N = N_0 P^k$ particles with energies $E = E_0 \beta^k$. Eliminating k between these two quantities, we have

$$\frac{N}{N_0} = \left(\frac{E}{E_0} \right)^{\ln P / \ln \beta}. \quad (2.10)$$

In fact, this value is actually $N(\geq E)$ since this is the number of particles with energy E and some fraction of them continue to be accelerated to even higher energies. Therefore,

$$N(E)dE = constant \times E^{-1 + (\ln P / \ln \beta)} dE. \quad (2.11)$$

Note that Eq. 2.11 is essentially equivalent to Eq. 2.9 with the primary difference being that while P and β are defined per cycle, α and τ_{esc} are defined per unit time. To find out β and P , we follow the arguments in Ref. [13, 25, 26]. Let us first determine the energy gain when the particle crosses from upstream to downstream. The gas on the downstream side approaches with a velocity $V = (3/4)U$ and so, performing a Lorentz transformation, the particle's energy when it passes into the downstream region is

$$E' = \gamma_V (E + p_x V) \quad (2.12)$$

where γ_V is Lorentz factor and p is the momentum of the particle. Here, the x-coordinate is taken to be perpendicular to the shock. The shock is assumed to be non-relativistic, so $\gamma_V = 1$, but the particles are relativistic and hence $E = pc$ and $p_x = (E/c) \cos \theta$. Therefore,

$$\Delta E = pV \cos \theta \quad \frac{\Delta E}{E} = \frac{V}{c} \cos \theta. \quad (2.13)$$

The probability that the particles which cross the shock arrive within the angles θ to $\theta + d\theta$ is proportional to $\sin \theta d\theta$ and the rate at which they approach the shock is proportional to the x-component of their velocities i.e. $c \cos \theta$. Therefore, the probability of the particle crossing the shock is given by $\sin \theta \cos \theta d\theta$. Normalising the probability distribution in the range $[0, \pi/2]$, we have

$$p(\theta) = 2 \sin \theta \cos \theta d\theta. \quad (2.14)$$

Therefore, the average energy gain in crossing the shock is

$$\left\langle \frac{\Delta E}{E} \right\rangle = \frac{V}{c} \int_0^{\pi/2} 2 \cos^2 \theta \sin \theta d\theta = \frac{2V}{3c}. \quad (2.15)$$

The particle's velocity vector is randomized without energy loss by scattering in the downstream region and it then recrosses the shock, when it gains another fractional increase in energy $(2/3)(V/c)$. Therefore, in making one round trip across the shock and back again, the fractional energy increase is, on average

$$\left\langle \frac{\Delta E}{E} \right\rangle = \frac{4V}{3c}. \quad (2.16)$$

Consequently,

$$\beta = \frac{E}{E_0} = 1 + \frac{4V}{3c} = 1 + \frac{U}{c}. \quad (2.17)$$

To calculate P , let us work in the frame of Fig. 2.5 (d). This is the rest frame of the downstream plasma. The upstream plasma is approaching the shock with a velocity $3/4U$ and the shock is moving into the upstream plasma at a velocity $U_2 = 1/4U$. Now, the particle velocity is isotropically distributed for the downstream plasma in this picture and let us denote the velocity component along the shock normal by (see Fig. 2.6)

$$v_n = v \cos \theta. \quad (2.18)$$

Only those particles will re-cross the shock which have $v_n < -U_2$. Therefore, to re-cross, θ must satisfy

$$-1 \leq \cos \theta \leq -\frac{U_2}{v}. \quad (2.19)$$

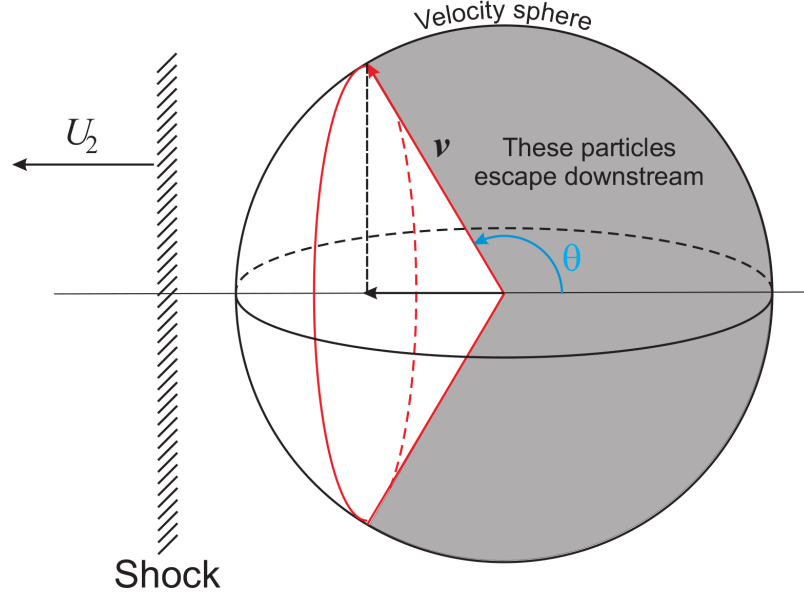


FIGURE 2.6: The velocities of particles in the rest frame of the downstream medium are nearly isotropically distributed over a sphere. Note that this figure is flipped with respect to Fig. 2.5 (d) and hence, the shock moves with velocity U_2 towards the left. Reproduced from Ref. [25]

Assuming an isotropic distribution in the downstream frame, the total flux across the shock, back into the upstream flow is given by

$$\mathcal{F}_u \propto \int_{-1}^{-U_2/v} d \cos \theta (v \cos \theta + U_2) = -\frac{(v - U_2)^2}{2v}. \quad (2.20)$$

The flux of particles away from the shock, further into the downstream flow, is due to particles with

$$-\frac{U_2}{v} \leq \cos \theta \leq 1. \quad (2.21)$$

The flux into the downstream flow is therefore proportional to

$$\mathcal{F}_d \propto \int_{-U_2/v}^{-1} d \cos \theta (v \cos \theta + U_2) = -\frac{(v + U_2)^2}{2v}. \quad (2.22)$$

The return probability, the chance that a particle ultimately finds its way back into the upstream flow once it is in the downstream flow, is the absolute value of the ratio of these two fluxes

$$P = \left| \frac{\mathcal{F}_u}{\mathcal{F}_d} \right| = \left(\frac{v - U_2}{v + U_2} \right)^2. \quad (2.23)$$

Assuming $v = c \gg U_2$ we have by approximation

$$P \approx 1 - \frac{4U_2}{c} = 1 - \frac{U}{c}. \quad (2.24)$$

Now using β and P from Eqs. 2.17 and 2.24, we have

$$\frac{\ln P}{\ln \beta} = -1. \quad (2.25)$$

Therefore, from Eq. 2.11, we have

$$N(E)dE \propto E^{-2} dE. \quad (2.26)$$

Finally, we have the result we have been seeking (due to reasons explained in Chapter. 1)– a power law of -2. This result, when first derived, excited a great deal of interest because it provided an excellent reason why a power law spectra with a unique spectral index should be found in diverse physical environments. The only requirements are the presence of strong shock waves and that velocity vectors of high energy particles are randomised on either side of the shock. [26]

Chapter 3

Simulation of DSA

In the last two chapters, we have come to know about the basics of CRs, particle acceleration and reviewed DSA in substantial detail. This chapter will focus on the technical details of CR Propa, the simulation setup used and at the end, layout a series of tests and initial calibrations that were performed with the code.

3.1 CR Propa

CR Propa is a simulation framework for efficient development of astrophysical scenarios for high energy particles. The upgraded and powerful third version of the code (CR Propa 3) was introduced in May, 2016 [5]. This section will lay out a broad outline of CR Propa 3 to the extent necessary for the purposes of this thesis. For a more detailed and thorough insight, have a look at Ref. [5].

The real power of CR Propa lies in the fact that it can deal with all the different aspects of cosmic ray propagation and interaction – such as galactic and extra galactic propagation, pair-production, photo-pion production, nuclear decay as well as various photodisintegration reactions. All these different aspects are handled via different modules and this modular structure makes CR Propa extremely easy to deal with and also extend according to one's own preferences. A visualisation of this modular structure is given in Fig. 3.1.

The cosmic ray candidate class incorporates all the information about the particle(s) in question – their charge, mass, velocity, energy, position etc. These candidates can be created either individually by the user by defining all these different parameters or they can also be produced by pre-defined source models wherein the user specifies the relevant properties of the source in question (such as the position, spectrum, composition etc.).

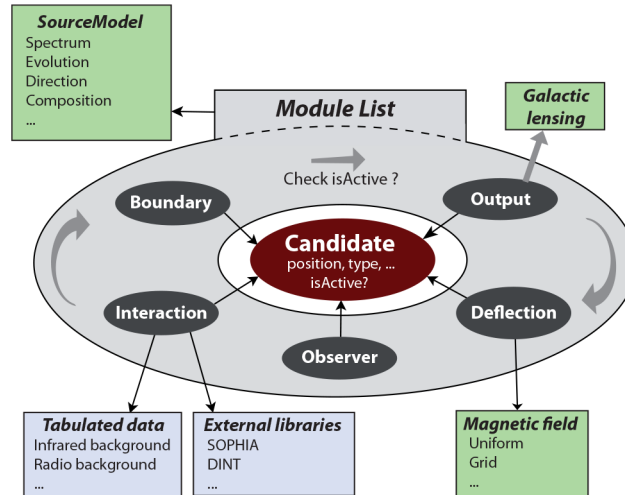


FIGURE 3.1: Illustration of the modular structure of CR Propa. Each module acts independently on the candidate class. The `isActive` flag serves as a user-defined break condition and is checked after each cycle of the module list. Reproduced from Ref. [5]

After creation, the various properties of the candidate(s) are updated at each simulation step as the various modules (eg. Propagation Module, Interaction Module) act one after another in the simulation and this continues in a cycle until a user-provided breaking condition is satisfied.

The modules have no direct dependencies on each other and hence in principle, it is possible to have a simulation with any combination of them allowing an extremely wide range of possibilities to be studied using this single framework. Besides, this independence of modules also means that modules can be replaced or removed at will and hence the framework can be extended or modified without having to worry about modifying other components.

The probability for various processes (for eg. an interaction) is calculated at each propagation step and to ensure that the step-size is small enough to process the different modules in one single step in any arbitrary order, the different modules bid for their own preferred step-size and the smallest bid wins.

Since interactions between cosmic rays are negligible, it is easy to parallelize a simulation by simply splitting it into smaller jobs. However, CRPropa 3 enables shared-memory multiprocessing using OpenMP¹. The actual simulation framework is written in C++ and interfaced to Python using SWIG². This, like many other recent frameworks, allows the user to script in a high level language like Python while all the actual computation under the hood is done with C++ code. The SWIG interface also allows for

¹www.openmp.org

²www.swig.org

cross-language polymorphism, which means that a user can directly extend a CR Propa simulation (for eg. by writing a new module) from the script that runs it.

All these features make CR Propa 3 an extremely useful tool and due to the motivations mentioned in Chap. 1, it is worthwhile to try to incorporate an acceleration module within CR Propa which implements DSA.

3.2 Simulation Setup

For this work, the inbuilt Source and Propagation modules of CR Propa were used and for the acceleration mechanism and observation/detection, custom modules were scripted, tested and deployed.

3.2.1 Geometry

To simulate DSA, we need to have a shock wave propagating through a diffuse medium, with a discontinuity in the properties of the medium on both sides of the shock front as shown in Fig. 2.5. All simulations were performed in the rest frame of the shock front (i.e. the situation shown in Fig. 2.5(d)). Since the whole purpose of this work is to show that DSA can be implemented in CR Propa and demonstrate the robustness of the code, the well-studied and simple rectangular “box” simulation setup was chosen. This is shown in Fig. 3.2

Since the simulation is performed in the rest frame of the shock front, it is stationary and is depicted by the grey plane with $U = 0$ in Fig. 3.2. There are two wire-frame boxes on both sides of shock front which show the upstream and downstream regions of the shock – the upstream gas flows into the shock front and the downstream gas moves away from it. Due to the arguments of Sec. 2.4, the velocity of the downstream plasma is chosen to be 1/4th of the upstream gas.

The red and the blue arrows are used to depict the motion of the “scattering centres”. The scattering centres represent the magnetic irregularities, which we spoke about in Sec. 2.2, from which the particles scatter. Now the question arises as to why the scattering centres move about in the same way as the plasma. This is due to something known as the “frozen flux” theorem of ideal MHD [29]. The theorem is actually valid for plasmas of infinite conductivity, however, it is logical to extend this to our case as a large section of the plasmas encountered in high energy astrophysics and astronomy, in general, have extremely high electrical conductivity [26]. The theorem states that in the limit of infinite conductivity, the magnetic flux is time invariant in a coordinate frame

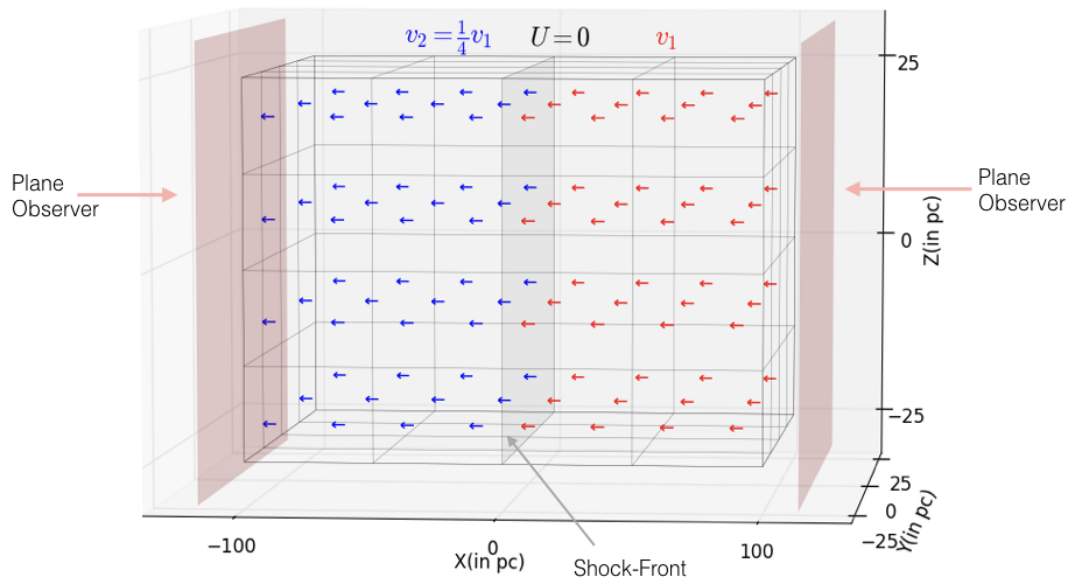


FIGURE 3.2: The simulation setup. The pink and the grey planes are the observer planes and the shock front respectively. The arrows depict the movement of the scattering centres on both sides of the shock front.

that moves along with the plasma – i.e. the magnetic field lines move in a plasma flow field in such a manner as if they have been frozen into the plasma as shown in Fig. 3.3. In our situation, we assume a plasma of infinite conductivity – hence the magnetic irregularities are frozen inside the plasma and they move in the same manner as that of the upstream and downstream plasma. Note that while this assumption may not represent the most realistic scenario, it is necessary for reproducing “textbook” DSA.

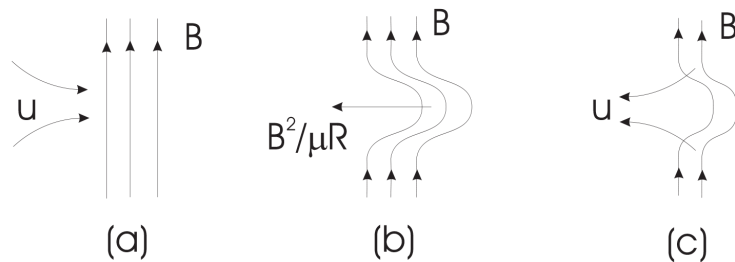


FIGURE 3.3: Magnetic field lines behave like elastic bands frozen into the fluid. (a) The relative motion between a conducting fluid (with a velocity u) and magnetic field lines give rise to induced currents (b) The induced current modifies the original field and the effect of the new field is that the fluid appears to be dragging the magnetic field lines along with it (c) The induced current interacts with the total field inhibiting further relative motion by a Lorentz force. Image reproduced from Fig. [29]

The wire-frame box represents the boundary of the acceleration region. The two XY planes and the two XZ planes of the wire-frame box are chosen to have periodic boundary conditions and hence in a sense, the acceleration volume is infinite in the Y and Z directions. The two pink infinite YZ planes are “plane observers” – they are placed

right outside the wire frame box (The distance between the planes and the box is exaggerated in the picture for aesthetic reasons). As was explained in Sec. 3.1, all CR Propa simulations need to have a user defined “break” condition and in our case, this break condition is the particle reaching either of these plane observers.

3.2.2 Methodology

The particles are injected into the acceleration region from an isotropic source emitting protons with an energy of 10 EeV. After the particles have been injected, our custom acceleration module is activated and the simulation progresses according to the flow chart shown in Fig. 3.4 till it is time for the particle to propagate, for which control is handed back to CR Propa’s propagation module.

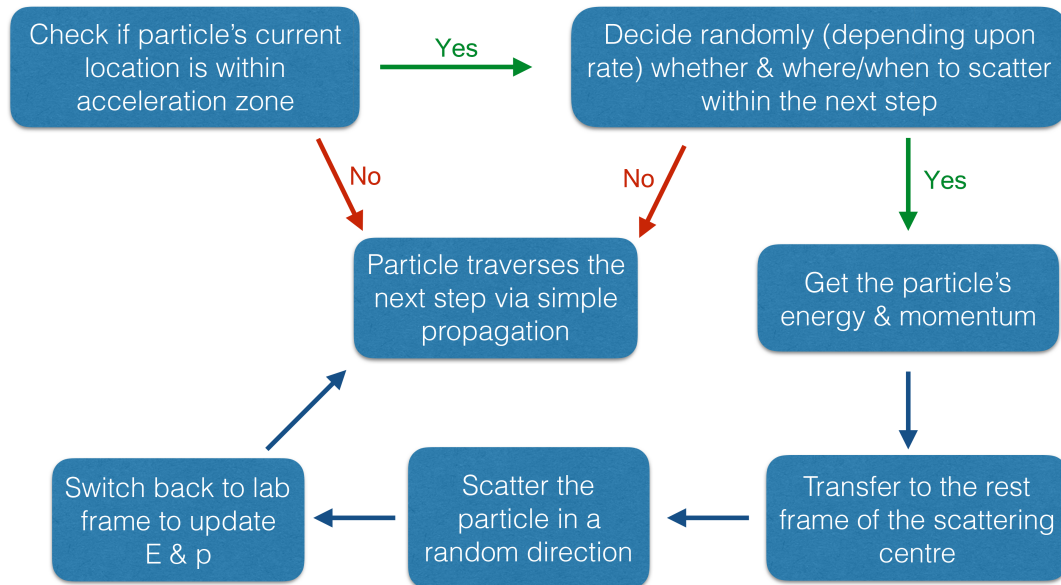


FIGURE 3.4: The scheme of operation of the Acceleration Module.

First, we check whether the particle is present within the acceleration zone at all and whether it “wants” to interact with a scattering centre within the next simulation step. Although the first decision question has a definitive answer, the second one is probabilistic and depends on the “current scattering rate”. (Note that the “current scattering rate” differs from the scattering rate which the user provides as an input because the rate depends on the location and motion of the particle. Therefore, it needs to be updated during every single simulation step when the decision question is invoked – this is elaborated in Sec. 3.2.3). If the answers to both the decision questions are positive, then the module goes ahead and performs the scattering. During this, the particle is scattered in a random direction while its energy is conserved – all in the rest frame of the

scattering centre. Thereafter, the control is handed to CR Propa’s “simple propagation module” by which the particle propagates an appropriate step length in a straight line. After this, the simulation again repeats the same cycle from the first step onward and this process continues recursively until the particle reaches either of the observer planes.

Therefore, the particle is moving in small steps and changing its direction continuously due to scatterings – it is effectively diffusing around in the simulation volume. It is important to note that while the particles don’t gain any energy from these scatterings in the rest frame of the plasma, their velocity distribution becomes isotropic in the rest frame because, during these scatterings, the particles are deflected in a random direction in the rest-frame of the scattering centre. Due to arguments of Sec. 2.4, we already know that this is exactly what is expected in DSA. By virtue of their motion, the particles cross the shock and whenever they do, they gain energy by Lorentz Transformations as shown by the detailed calculations in Sec. 2.4.

The process described above successfully mimics all aspects of DSA – particles are injected into the acceleration region, they gain energy whenever they cross the shock front and after crossing the shock either from upstream to downstream or vice versa, their velocity distribution is isotropized via scatterings off magnetic irregularities.

3.2.3 Modification of the Scattering Rate

If a particle undergoes n scatterings while traversing a distance d , then the scattering rate is defined to be n/d . Thus, it can also be defined as the inverse of the mean distance travelled by the particle in between two scattering events i.e. essentially the inverse of the mean free path. Since we perform the simulation in the rest frame of the shock, the scattering centres are not stationary both upstream and downstream. In such a scenario, the scattering rate depends on the relative motion between the particle and the scattering centres. In fact, in this simulation, the macroscopic properties such as temperature, density are not tracked – therefore, the only thing which differentiates the upstream and the downstream region is the different velocity and direction of motion of the scattering centres and hence the different effect they have on the scattering rate.

To see how the scattering rate varies, let us take a look at Fig. 3.5. The dot at the centre of the image represents the position where the particle had its last scattering. Let the average separation between two scattering centres be d and hence the next scattering centre can be anywhere on the drawn sphere of radius d . Some representative scattering centres are shown on the surface the sphere and let us assume that all the scattering centres are moving towards the $-x$ direction with a velocity \vec{u} . Let the particle be moving with a velocity \vec{v} as shown in the figure. Let us try to find out the number scatterings

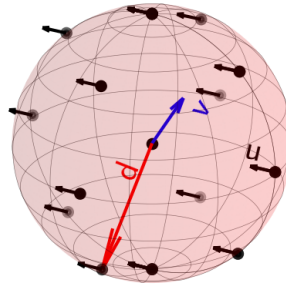


FIGURE 3.5: Motion of Scattering centres. The central dot depicts the location of the last scattering. The dots on the sphere represent moving scattering centres.

undergone by the particle in traversing the distance d . This is given by

$$n = \rho \tau (|\vec{v}| - \vec{u} \cdot \hat{v})$$

where $\tau = d/|\vec{v}|$ is the time taken by the particle to traverse the distance d and $\rho = 1/d$ is the linear density of scattering centres. Therefore plugging these values in, we obtain the scattering rate

$$R = \frac{n}{d} = \frac{|\vec{v}| - \vec{u} \cdot \hat{v}}{d|\vec{v}|}. \quad (3.1)$$

If the scattering centres were stationary, then the scattering rate would have been simply $1/d$. Hence, the “initial scattering rate” or the scattering rate that is provided as a user input $1/d$ needs to be modified by the factor $(|\vec{v}| - \vec{u} \cdot \hat{v})/|\vec{v}|$. As this factor is not constant for all simulation steps, the rate needs to be calculated at each propagation step as described in Sec. 3.2.2.

3.3 Calibration & Initial Checks

Fig. 3.6 shows the trajectories for two simulated particles. The particles are dispatched from an isotropic source $30 pc$ away from the shock front in the upstream region. In both cases, the particles move around the simulation volume crossing the shock multiple times (which can be seen clearly from the angle presented in Fig. 3.6(b)) before getting detected by the left observer plane. It is not coincidence that both the particles demonstrated here are detected by the left observer and they seem to be penetrating not too much into the upstream – in fact, a quick glance at Fig. 3.2 should make the reason clear to the intuitive reader. When the particle crosses the shock from the downstream to the upstream region, the particle has the tendency to get advected by the flow of the

plasma towards the shock. Therefore, most of the trajectories are of the nature shown in Fig. 3.6 – they rarely get detected by the upstream observer.

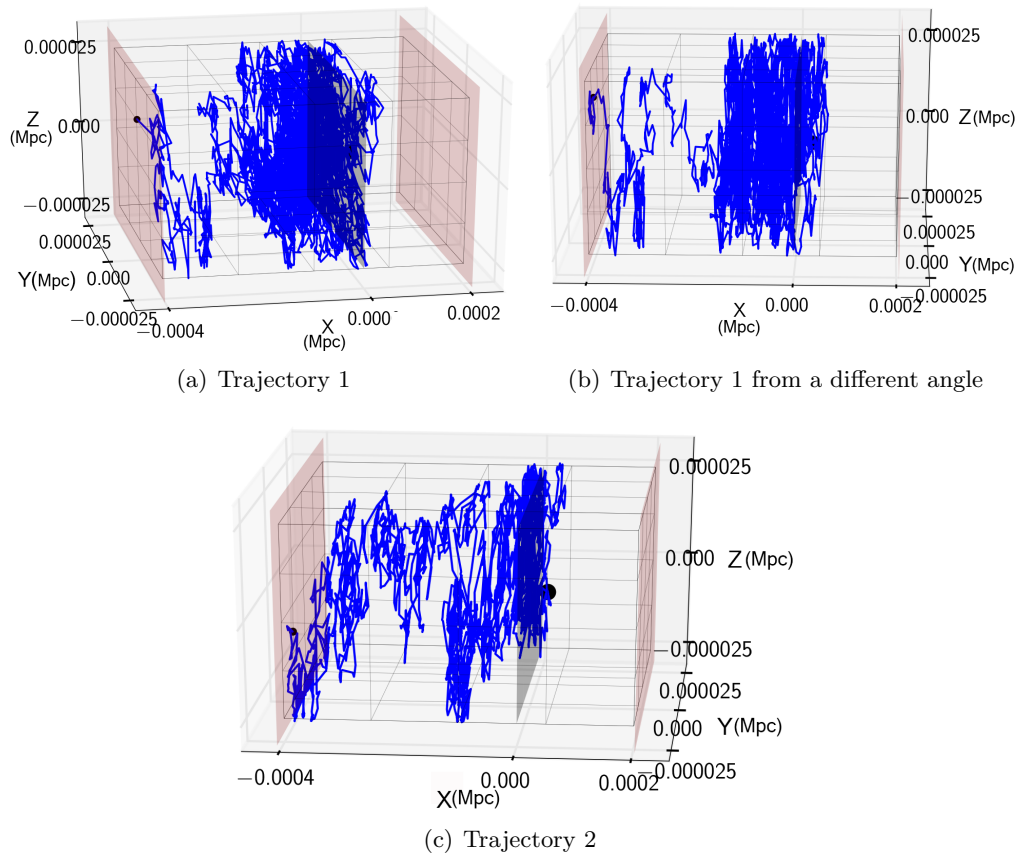


FIGURE 3.6: Two particle trajectories. The big black blob in the upstream box is the source and the black dot on the downstream observer happens to be the point of detection

In fact for such box-acceleration scenarios, it is almost always assumed while performing analytical calculations that no particles exit the acceleration region upstream. Therefore, to make sure that holds true for our simulation as well, we must make our upstream simulation volume long enough so that all or most particles can't reach the upstream observer. But making the simulation volume longer also increases the computation time and hence we have to choose a value for the length of the upstream box, so that a substantial majority of the particles get detected by the downstream observer. To this end, 8 simulations with different lengths for the upstream box were performed for 1000 particles each with an input scattering rate of $1/(4pc)$. The number of particles detected by both the observers is shown in Fig. 3.7

From $100 pc$ onward, the number of particles detected by the upstream observer is ≤ 10 i.e. $\leq 1\%$. Note that the y-scale is log and hence the count going up for $200 pc$ is just a statistical fluctuation. Therefore, a choice of $200 pc$ for the right box ensures that the

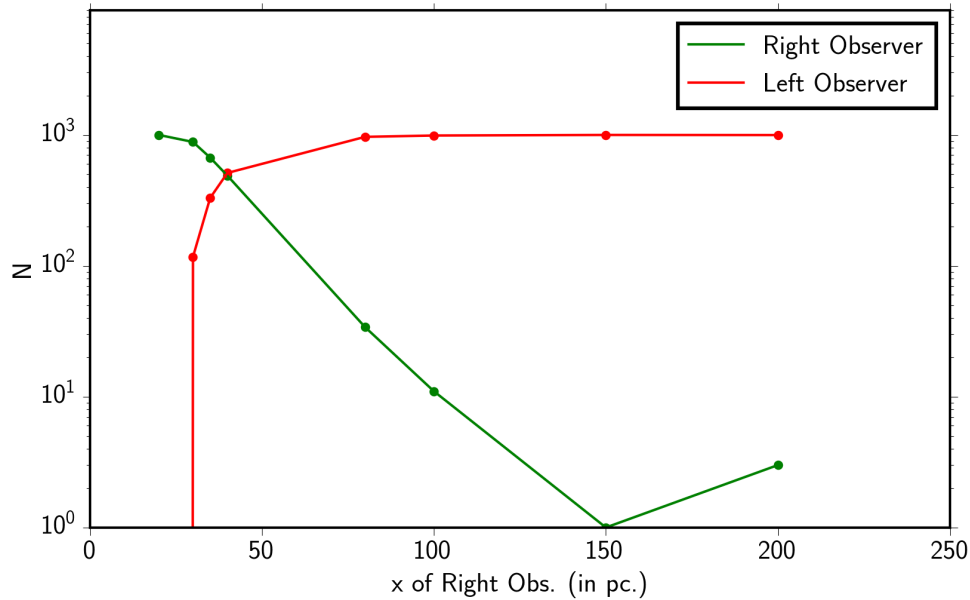


FIGURE 3.7: The number of particles detected by each observer. Right Observer refers to the upstream observer and left refers to the downstream one.

box is not too long, but still ensures most of the particles exit the acceleration region downstream. For all the simulations performed in this work, the upstream observer is always kept at 250 pc unless mentioned otherwise and for all these cases $\leq 0.7\%$ of the particles are detected upstream.

The choice of the size of the downstream box is more involved and will be expanded upon in Chapter 4.

The above tests and calibration have made sure that the particles after being emitted from the source are moving around the simulation volume and getting detected as expected. To demonstrate that the particle dynamics are also coherent with the physics, a plot of the energy and the trajectory lengths for 60 particles are shown in in Fig. 3.8.

All the particles are injected at 10 EeV and hence, all of the particle traces begin from the left-lower corner of Fig. 3.8. Then, as the particle moves around, it gets scattered and the trajectory length keeps on increasing – these are represented by the horizontal lines in the image. Whenever the particle crosses the shock front it gains energy without traversing much distance and hence these are represented by the near vertical lines in the image. Therefore the particles dynamics are as expected – the particle moves around interacting continuously with the scattering centres and gaining energy during shock crossings.

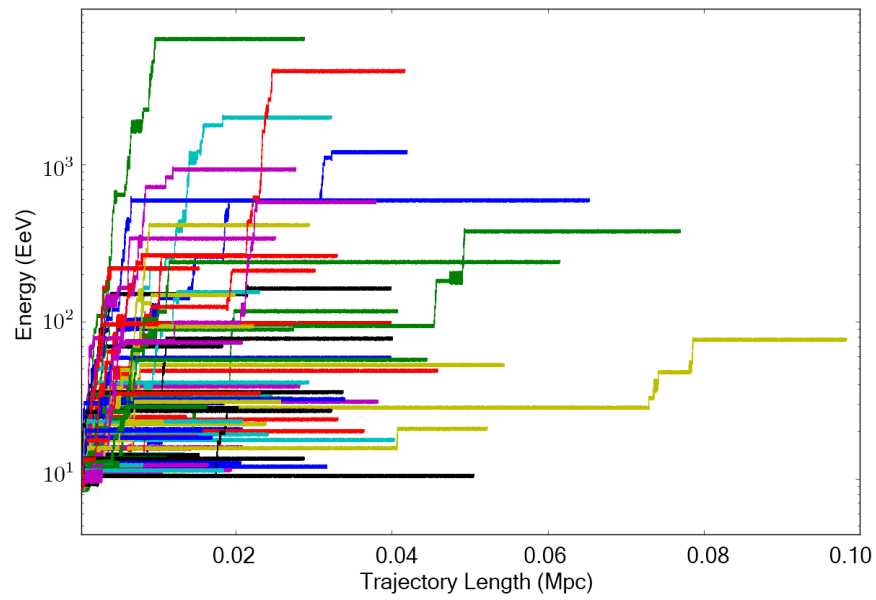


FIGURE 3.8: Energy and trajectory length for 60 particles. Different colours represent different particles.

The location of the source was moved around the simulation volume and was found to have no substantial effect on the results of the simulation. Therefore, to ensure that most particles cross the shock at least once, it is placed in the upstream region and to reduce simulation run time, it is not placed too far away from the shock-front.

Chapter 4

Results

This chapter has been broken down into various sections according to what aspect of DSA they deal with. Some of them deal with the geometry of the acceleration, some with the mechanism, some with how to extend DSA and a last section demonstrating how the results of this work may be applied to experimental data.

To prevent repetition, a set of default simulation parameters and their values are defined in Table 4.1 – these are the values used in all instances of the simulation unless mentioned otherwise explicitly.

Parameter	Symbol	Default Value
Right/Upstream Box Size	L_{rbox}	250 pc
Upstream Scatter Centre Velocity	v_1	0.1 c
Downstream Scatter Centre Velocity	v_2	0.025 c
Input Scattering Rate	R	1/(4 pc)
Source Type	–	Isotropic
Source Energy	E_{src}	10 EeV
Source Position ¹	x_{src}	(30, 0, 0)pc
Particles in each simulation	N	10000

TABLE 4.1: Default Simulation Parameters. [1] The origin of the axis is at the centre of the shock front and the axes are oriented as shown in Fig. 3.2.

4.1 Downstream Box Size

As explained in Sec. 1.3, one of the most powerful features of DSA happens to be the fact that it inherently results in a power law with a spectral index of -2.0 . Thus, if the simulation is working as expected, the spectrum of the simulated particles should also be a power law with a -2 spectral index. Figure 4.1 shows the spectrum obtained for a simulation with the default parameters of Table 4.1. The lower half of the figure

represents the energy spectrum i.e. the number of particles as a function of the energy, while the upper half is the differential energy spectrum i.e. $\frac{\text{number of particles}}{\text{bin-width}} * (\text{Energy})^2$ as a function of the energy. The differential energy spectrum is preferable in this case because if a certain spectrum has the power law E^{-2} then it will be represented by a horizontal line and thus it is easy to notice, even before fitting, whether one has a spectrum with a power law of -2 or something harder or softer.

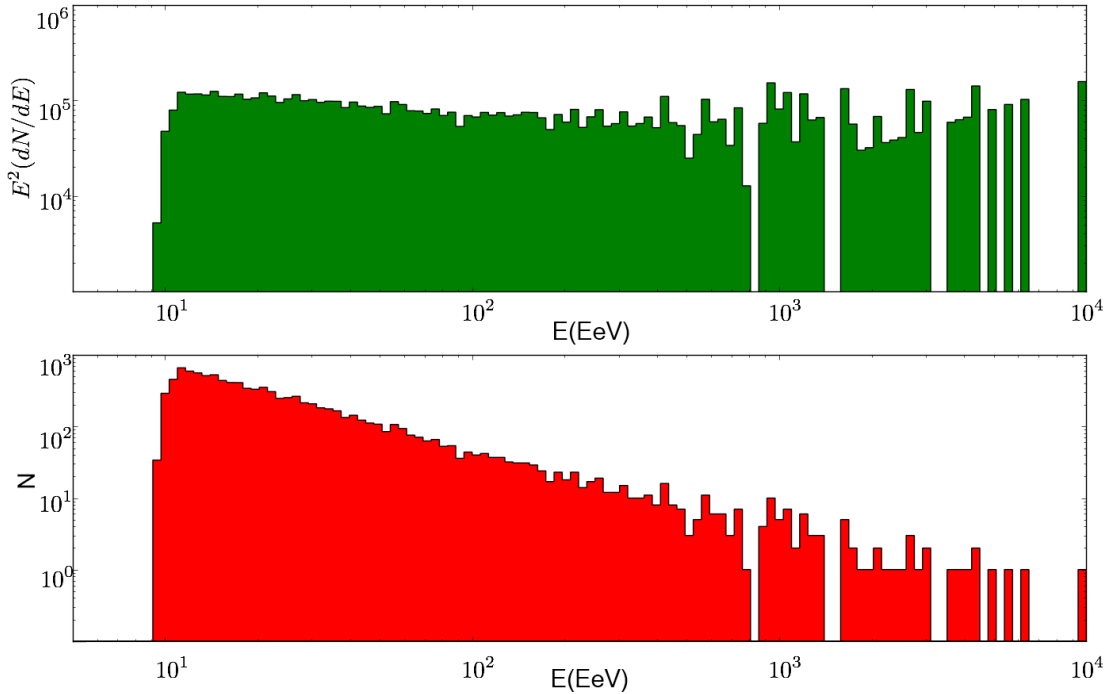


FIGURE 4.1: The spectrum for a simulation with standard parameters and $L_{box} = 100$ pc. Lower pane represents the energy spectrum i.e. the number of particles as a function of the energy, while the upper pane is the differential energy spectrum i.e. $\frac{\text{number of particles}}{\text{bin-width}} * (\text{Energy})^2$ as a function of the energy.

As is obvious from the differential energy spectrum of Fig. 4.1, the simulated spectrum is softer than a power law of -2.0 . One of the parameters that are not mentioned in Table 4.1 happens to be the size of the left box/downstream box (L_{box}) and it is taken to be 100 pc for the above simulation. Let's increase that size to 200 pc. The spectrum obtained with such a parameter is shown in Fig. 4.2.

It is clear that Fig. 4.2 has a harder spectrum than Fig. 4.1 and it is close to the theoretically predicted spectrum. A power law fit (shown in Fig. 4.3) assuming Poisson errors, reveals an index $x = -2.0452 \pm 0.0117$ i.e. a spectrum slightly softer than the DSA spectrum. .

It is clear from the above two cases that the size of the downstream box directly affects the spectrum. Hence, the simulation was performed for various sizes of the downstream box and the results are shown in Fig. 4.4. For $L_{box} = 40$ pc, the index is -2.89 and then

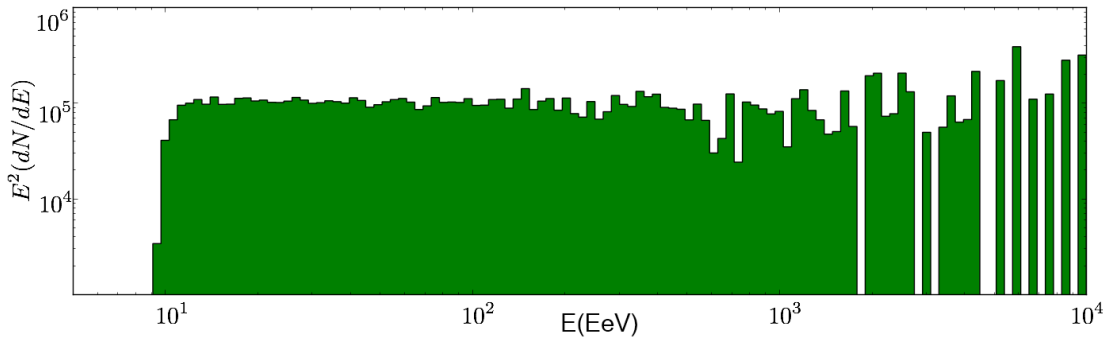


FIGURE 4.2: The spectrum for a simulation with standard parameters and $L_{lbox} = 200$ pc

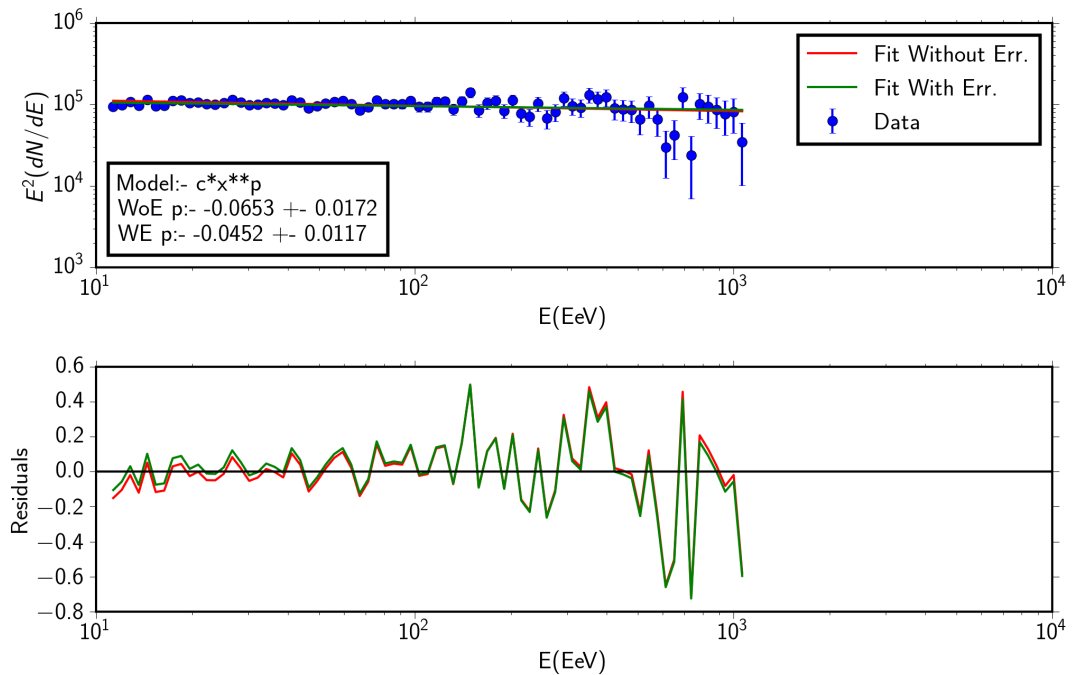
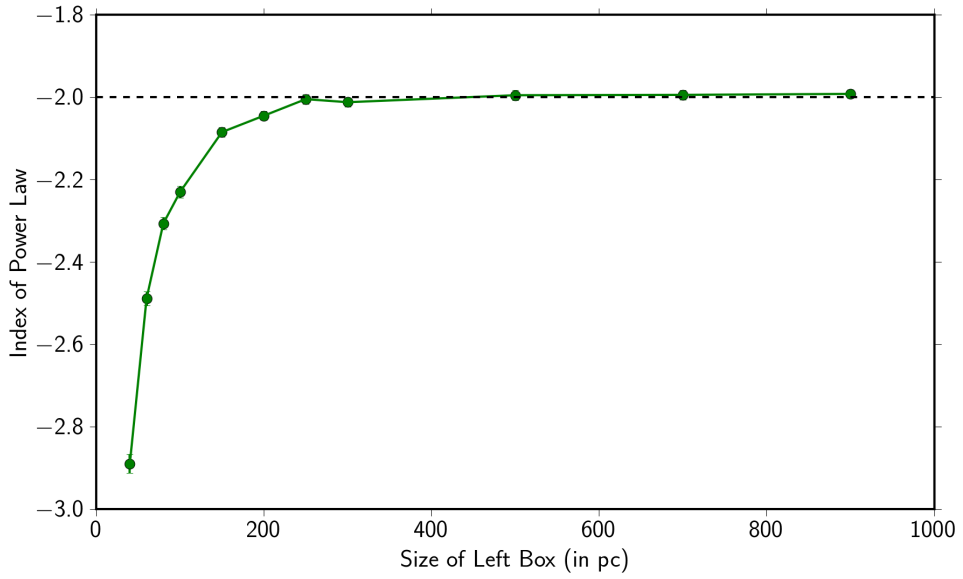


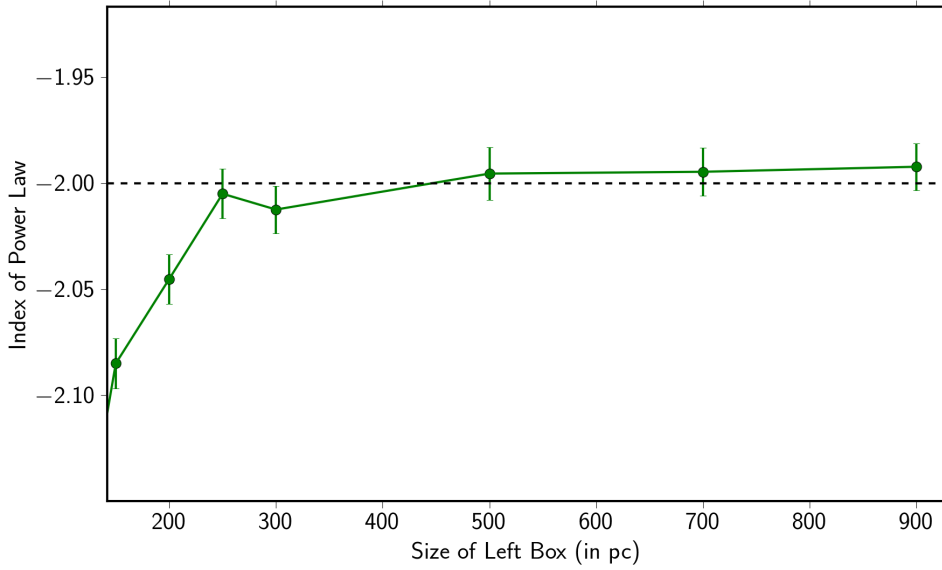
FIGURE 4.3: The best fit and residuals for the spectrum shown in Fig. 4.2. The green line shows the fit when Poisson errors are assumed on the simulated values and the red line shows the fit without errors. “WoE p” refers to the deviation of the index from -2 when no errors are taken into account and “WE p” refers to the deviation when errors are taken into account.

it rises rapidly finally appearing to “stabilise” exponentially towards -2.0 for $L_{lbox} \geq 250$ pc.

The existence of something like a “critical length” for the downstream box to obtain the canonical spectral index can be connected to the escape probability. If we place the left observer too close to shock front, then a particle which might have otherwise returned to the shock is now removed from the simulation, thus introducing artificial effects. When the left box is made long enough, at large distances from the shock front, the return probability of the particle is so small that even removing it artificially



(a)



(b)

FIGURE 4.4: The index of the power law for various sizes of the downstream box/left-box. (b) zooms into the region of (a) close to a -2.0 power law

from the simulation does not have a substantial effect. The fact that this is indeed the cause behind the index changing with L_{lbox} can be verified by monitoring the escape probability of the particles as we change the box-size. The escape probability should go down as L_{lbox} increases and it will be demonstrated that this is indeed the case in Sec. 4.2. For all simulations hereafter, it should be assumed that a stable value of L_{lbox} has been chosen unless mentioned otherwise.

4.2 Relative Energy Gain & Return Probability

It was demonstrated in Sec. 2.4 that the energy gain factor β and the return probability P in DSA vary as $\beta = 1 + \frac{U}{c}$ (Eq. 2.17) and $P = 1 - \frac{U}{c}$ (Eq. 2.24). It is possible to measure both β and P in the simulation.

For measuring β , the code records the particle energy every time the particle crosses the shock. Let the particle energy measured during a shock crossing be E_1 . After the particle has completed one full-cycle thereafter (i.e. on the 3rd crossing since the initial one), let its energy be E_3 . Then

$$\frac{\Delta E}{E} = \frac{E_3 - E_1}{E_1}. \quad (4.1)$$

Thereafter, β can be calculated using Eqs. 2.16, 2.17. Note that this gives $(\Delta E/E)$ for a full cycle; if we measure the energy during the very next crossing after the first crossing (i.e the second crossing), then similarly, we can calculate $(\Delta E/E)$ for half a cycle as well.

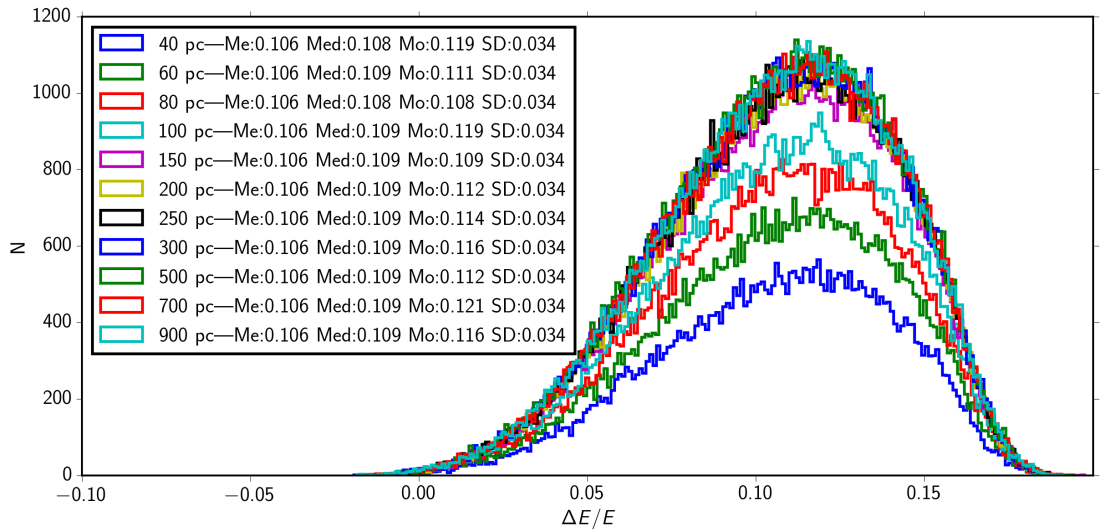


FIGURE 4.5: Distribution of $(\Delta E/E)$ for various box sizes. Here Me denotes the mean, Med the Median, Mo the mode and SD the standard deviation.

Fig. 4.5 shows the distribution of $(\Delta E/E)$ obtained for various values of L_{box} . During each shock cycle, different particles approach the shock-front with different angles and hence they end up gaining slightly different amounts of energy because of the presence of the angle in the Lorentz Transformation (Sec. 2.4). From Fig. 4.5, it is clear that all the distributions have a mean close to the theoretically expected value of 0.1 for this case. All the distributions have the same nature, as changing L_{box} does not affect the energy gain per cycle – it only affects the escape probability as described at the end of Sec. 4.1.

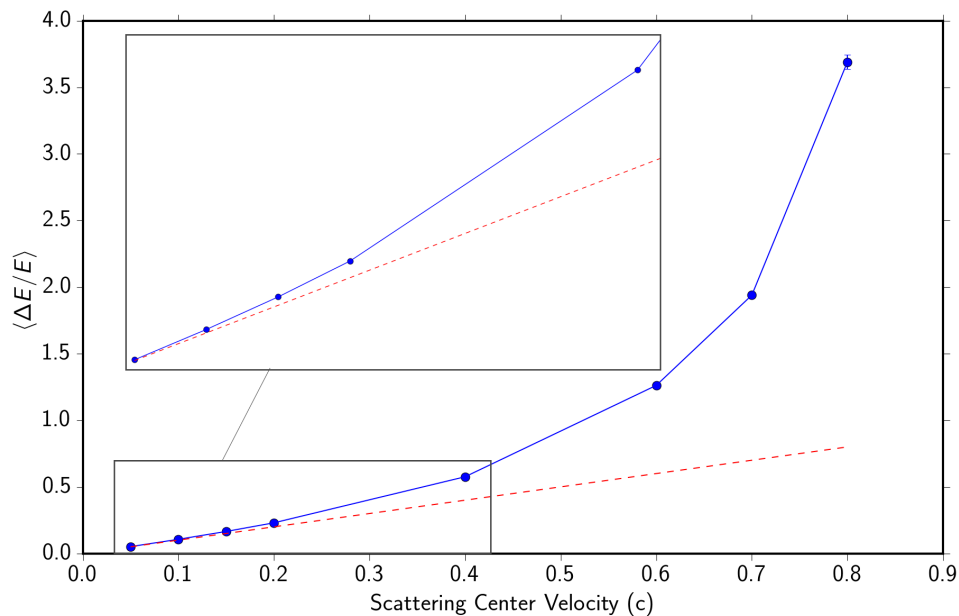


FIGURE 4.6: Mean value of $\langle \Delta E/E \rangle$ for various values of the upstream scatter centre-velocity in the simulation frame i.e. the shock velocity in the “lab” frame. The red-dotted line refers to the theoretically expected value for non-relativistic shocks. The inset shows the region where the simulated values are close to the theoretically expected values

To verify Eq. 2.16, the simulation is repeated for various values of shock velocity and the result is shown in Fig. 4.6. The simulated values are close to the theoretically expected values for smaller shock velocities. However, as the shock velocity increases, the simulated values diverge quickly away from the theoretical calculations. Increasing the shock velocity moves us into the domain of relativistic and ultra-relativistic shocks and it has already been predicted [16] that DSA is not the operating mechanism for such shocks. In such cases, the anisotropy in the angular distribution of the accelerated particles is so large upstream that the spatial diffusion approximation breaks down and hence, our treatment of DSA does not apply anymore. Thus, our simulation is consistent with these expectations and shows that the relativistic effects clearly become visible for values of shock velocity greater than $0.4c$.

Till now, $\langle \Delta E/E \rangle$ for a full shock cycle has been dealt with. However, the distribution of $\langle \Delta E/E \rangle$ for half a cycle also provides a delightful insight into the energy gain during individual shock crossings. Fig. 4.7 shows the distribution of $\langle \Delta E/E \rangle$ for half a cycle with a shock velocity of $0.1c$. We argued in Sec. 2.4, how the particle gains energy in each shock crossing. However it is important to realise that such an argument is only valid when we constantly keep switching between the upstream and downstream frames as the particle makes the crossings. In the rest frame of the shock (i.e. the rest frame of the

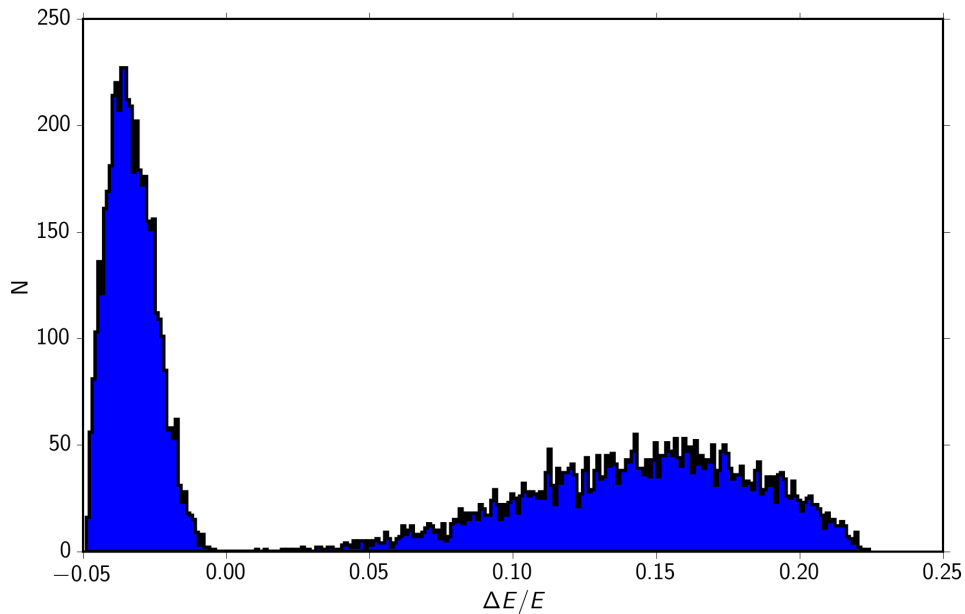


FIGURE 4.7: The half-cycle distribution of $(\Delta E/E)$ for a shock velocity of $0.1c$

simulation), when the particle crosses from downstream to upstream, it has a head-on collision and it gains energy while it loses energy during the tail-on collision while going from upstream to downstream. The left peak in Fig. 4.7 represents particles crossing from upstream to downstream while the right peak depicts the opposite scenario. Due to the magnitudes of the energy loss and gain involved, during a full cycle a particle always ends up gaining energy.

To calculate P in the simulation, the code keeps track of how many times each particle crosses the shock-front. Let us assume that the source in the upstream region emits N_0 particles. All these eventually make their way downstream as no particle can escape upstream. Now, out of these N_0 , let N_1 particles escape and $N_0 - N_1$ return to the shock. Note that these N_1 particles have crossed the shock only once, while all the others cross the shock at least twice. Therefore, the probability of staying in the box/returning to the shock is given by

$$P = 1 - \frac{N_1}{N_0}. \quad (4.2)$$

Fig. 4.8 shows the value of P obtained via simulation for various values of the shock-front velocity/upstream scattering centre velocity. Just like Fig. 4.6, here also the simulated values are close to the theoretical values for low values of v_1 and diverge for $v_1 \geq 0.4c$. As explained earlier in this chapter, this is due to the fact that DSA is no longer applicable for (ultra)-relativistic shocks.

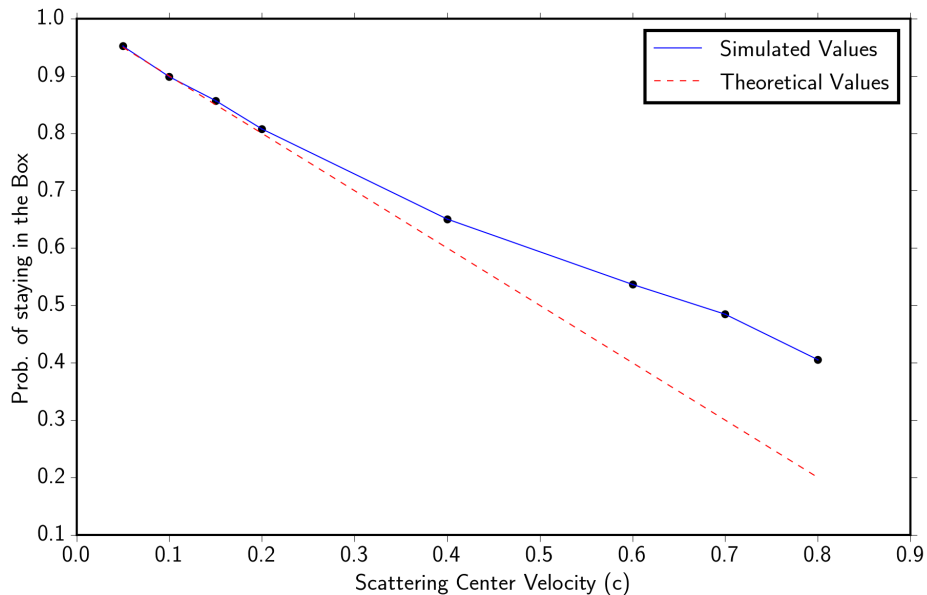


FIGURE 4.8: P for various values of the upstream scattering centre velocity. The red dotted line refers to the theoretical values for the non-relativistic case.

Fig. 4.9 shows P for various sizes of L_{lbox} . For 40 pc, P is 0.82 and it quickly rises and stabilises around the theoretical value of 0.9 around $L_{lbox} = 200$ pc. This proves our previous claim in Sec. 4.1 that the change in index of the spectrum with L_{lbox} is due to a modification of the escape probability of the particles with the size of the downstream box. A smaller downstream box size means a higher escape probability and vice versa.

4.3 Mean Free Path

In Sec. 3.2.3, the scattering rate was defined to be the inverse of the mean free path (MFP). As laid out in Table 4.1, for all the simulations reported on till now, an “input” value of 4 pc was used for the MFP. At first instance, it might seem that since MFP directly affects the scattering rate, a different input value of MFP will result in different dynamics and hence will alter the spectrum. However, the MFP is just an indication of the scale of the simulation and just like any other computer simulation, there is no preferred scale and the results remain the same irrespective of scale.

Figure. 4.10 demonstrates how the results of the simulation remain unaffected by different input values of the MFP. For generating this image, the simulation was run for $MFP = 2$ pc, 4 pc and 10 pc and the left box-size was varied as 60 pc, 80 pc, 100 pc and 150 pc for each of the MFP values. All these simulations produced power laws and the indexes are shown in the figure. The selection of these values ensures that we perform

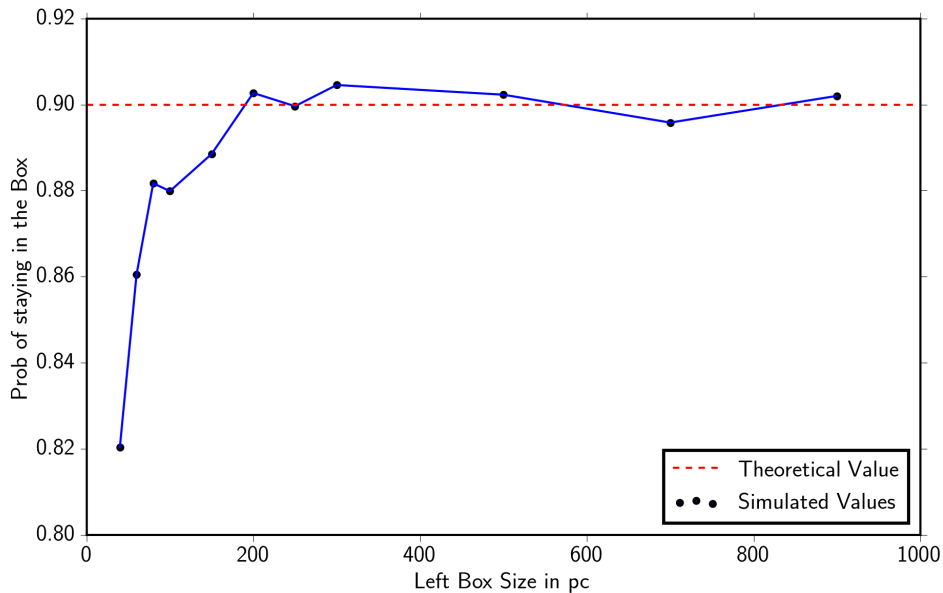


FIGURE 4.9: P for various values of L_{lbox}

the simulation for a wide range of values for the parameter (Left Box Size/MFP). As Fig. 4.10 demonstrates, this is the parameters that matters and not the absolute size of the downstream box as one might think from Sec. 4.1. After all, for a smaller value of MFP, the particle needs a smaller simulation volume for its velocity to become isotropic and vice-versa.

4.4 Energy Dependent Scattering Rate

In the first few sections of this chapter, it has been established to substantial detail that the results of our simulation are consistent with the picture of standard “textbook” DSA – thus, it can be said that we have successfully incorporated DSA within CR Propa and our simulation framework is quite robust. However, DSA in actual physical scenarios is much more complicated than the simple textbook case. In this section and the next one, two such realistic additions will be made to the simulation in order to see how the results vary from textbook DSA.

It was shown in Sec. 3.2.3, that the scattering rate is varied dynamically within the simulation by the location and direction of the particle. In realistic scenarios, the MFP and hence the scattering length also scales with the energy of the particle. Besides CR scattering, magnetic field turbulence has implications for many other astrophysical scenarios such as cloud chemistry, radio wave scattering through ionized medium [30]

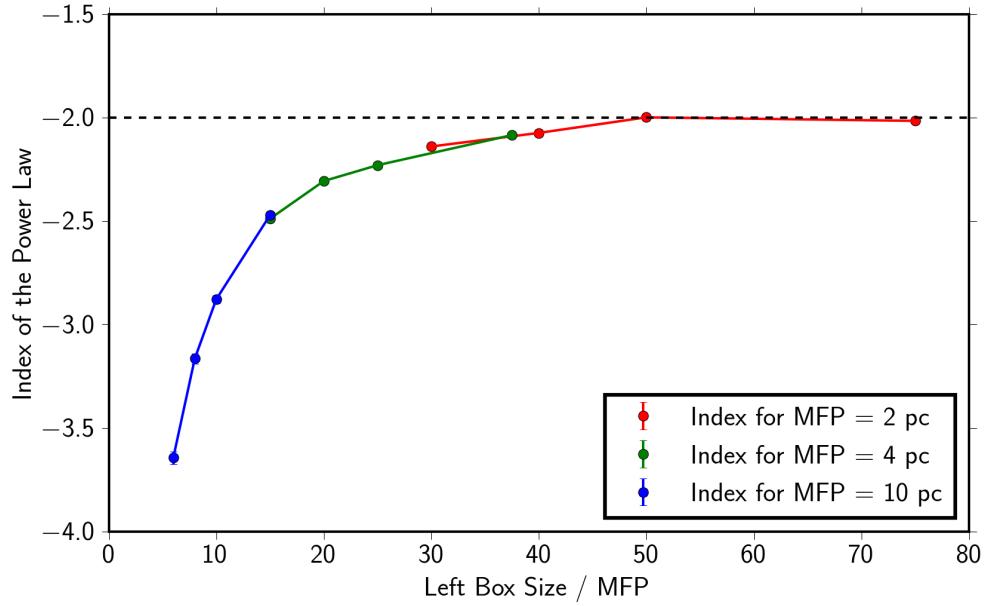


FIGURE 4.10: Index of the Power Law spectrum for different values of (Left Box Size/MFP)

and hence has been studied in great detail. Most theoretical studies of CR scattering derive the relevant results by relying on macroscopic tools such as the Fokker-Planck equation, transport equation etc. It has been demonstrated in Ref. [30, 31] that for CRs travelling through a background medium that moves with a non-relativistic bulk speed parallel to an ordered magnetic field B_0 with superposed Alfvén waves propagating parallel and/or anti-parallel to B_0 , the mean free path for a particle with energy E and charge Z varies as

$$\lambda \propto \left(\frac{B}{\delta B}\right)^2 (R_G k_{min})^{1-q} R_G \equiv \lambda_0 \left(\frac{E}{1 \text{ EeV}} \frac{1}{Z}\right)^{2-q} \quad (4.3)$$

where k_{min} is the minimum Alfvén wave number in the system, δB is the strength of the irregularities, R_G is the gyro-radius of the particle and q is the turbulence index of the magnetic field. Fig. 4.11 shows the indexes of the power-law spectrum obtained with different box-sizes. The nature of the variation, in this case, is the same as that of the standard scenario, however, the curve now levels off to a value of -2.16 instead of -2 i.e. energy dependent step-size/MFP results in softer spectra. For an energy dependent MFP, as the particle gains more and more energy it travels in larger and larger steps (i.e. energetic particles need to traverse more distance to alter their direction) – this alters the escape probability that is calculated in Sec. 2.4 and hence the results differ from that of the standard scenario.

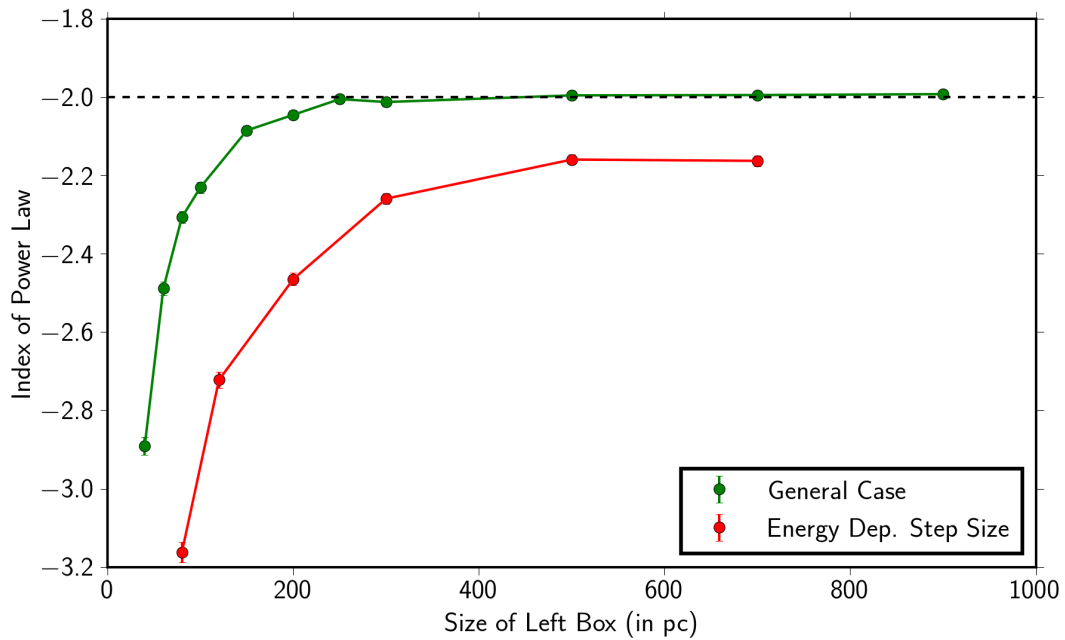


FIGURE 4.11: Indexes of the power law spectrum for standard and energy dependent scattering rate. For the energy dependent scattering rate, the input mean free path (i.e. λ_0 of Eq. 4.3) is 4 pc for all cases.

4.5 Variable Scatter Centre Density

Till now, it has been assumed that scattering centres are present uniformly throughout the acceleration region – however, this may very well not be the case in a real-life scenario. In this section, we will deal with the effects of replacing this uniform distribution with a Gaussian distribution of scattering centres centred around the shock-front. Although this may not be the most realistic assumption, it is a reasonable first-step assumption. In a sense, under this scheme, the shock now has a structure and a definite “width” consisting of scattering centres that go down in density as the distance from the shock-front increases. Let us define the shock-width to be the standard deviation(σ) of the Gaussian distribution of scattering centres.

Fig. 4.12 shows the power law indexes obtained for Gaussian distributions with various standard deviations. For each σ , the simulation is run over a range of downstream box-sizes. All the different shock-widths produce results of the same nature, however, the spectrum in the stable region become softer as the shock becomes narrower. Just like in Sec. 4.4, here also, the results differ from “textbook” DSA because the modification we have introduced alters the escape probability calculated in Sec. 2.4. In fact, in this case, the varying distribution of scattering centres also has an effect on the situation in the upstream box. As the shock becomes narrower, a large number of the scattering centres become concentrated in a small region near the shock – thus once a particle has been

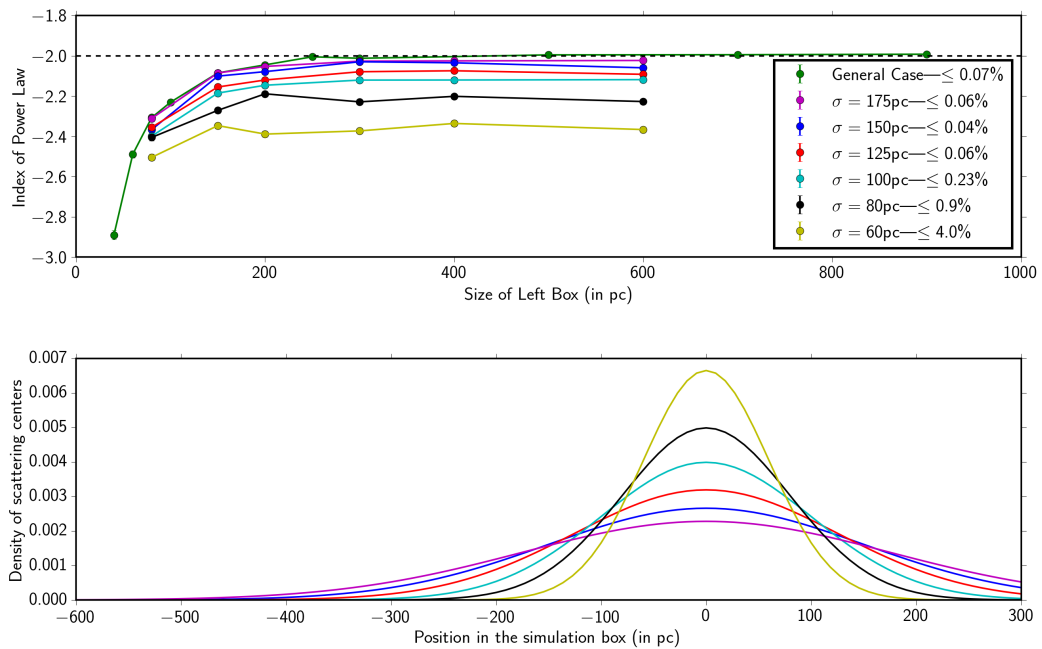


FIGURE 4.12: The top figure shows the indexes of the power law spectrum for various shock widths. The corresponding percentages in the legend box refer to the percentage of total particles that are detected by the upstream observer. The bottom figure shows the corresponding normalized scattering centre distributions

able to make its way through this dense region, there is almost nothing stopping it from exiting the simulation volume using the upstream exit. For this purpose, to ensure lower rates of particle leakage, $L_{r\text{box}}$ is increased to 400 pc for all these simulations. With this, it was possible to achieve a particle leakage rate of $< 1\%$ for all shock widths except 60 pc.

It should be mentioned that the results of Fig. 4.12 is for a scattering rate with no energy dependence. If we turn on energy dependence, then the results that we get are shown in Fig. 4.13. Note that the shock widths for which the simulation is performed is not the same in both cases.

As demonstrated in Figs. 4.11, 4.12 an energy dependent scattering rate and a Gaussian distribution of scattering centres around the shock front both lead to softer spectra. With both these features combined, the effect on the simulation seems to be more pronounced, producing even more softer spectra than one might expect by a linear addition of these two effects. As should be clear from the comparison of the percentages listed in Figs. 4.13 and 4.12, an energy dependent step size makes the leakage problem even worse. As high energy particles now have a larger step size, it is easier for them to cross the narrow region of scattering centres near the shock front without many interactions and thus

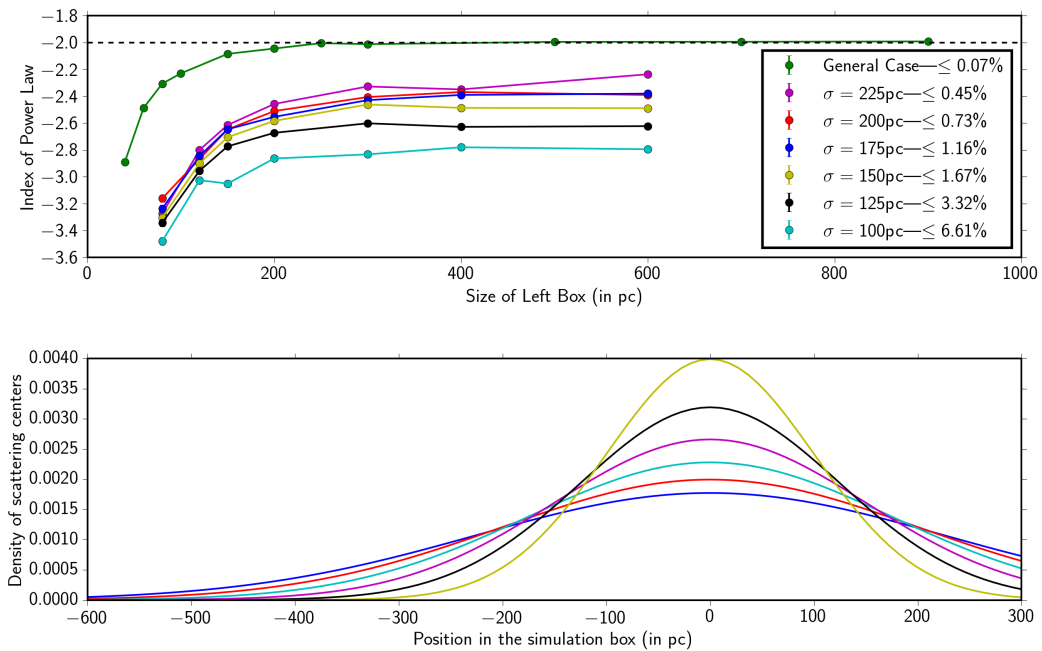


FIGURE 4.13: The top figure shows the indexes of the power law spectrum for various shock widths with an energy dependent scattering rate. The corresponding percentages in the legend box refer to the percentage of total particles that are detected by the upstream observer. The bottom figure shows the corresponding normalized scattering centre distributions.

escape upstream. Thus even with $L_{rbox} = 400$ pc, in this case for all $\sigma \leq 175$ pc, we have a leakage rate greater than 1%.

Fig. 4.14 summarises all the information in this section. It shows the indexes of the power law for various shock-widths for $L_{lbox} = 400$ pc (which is within the stable region as Figs. 4.11, 4.12 show). Therefore, these are the index values which are asymptotically approached by each of the corresponding spectra. This “levelling off” value increases with shock-width for both cases as shown in Fig. 4.14 with the energy-independent case seeming to reach the standard -2.0 for an infinite shock-width.

There is another difference between the standard case and the scenario presented in this section which is not apparent until one compares the particle energy spectra for both cases for a stable size of L_{lbox} . It is clear from the pictures listed in the Appendix² (for eg. Figs. A.2 and A.10) that while in the standard case, particles are always accelerated almost up to 10^4 EeV (with an injection energy of 10 EeV) for a stable downstream box-size, the spectrum for the cases with a Gaussian distribution of scattering centres have a cut-off much earlier in the energy range and the location of the cut-off depends on the shock-width and whether the scattering rate is energy dependent or not. Fig. 4.15 shows

²The spectra for a few cases from each scenario described in this thesis is listed in the Appendix

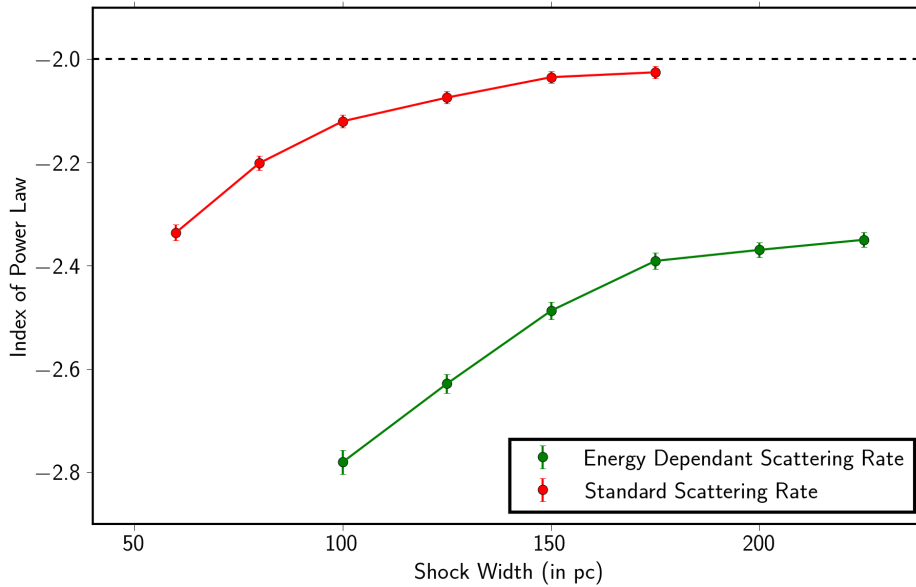


FIGURE 4.14: The indexes of the power law for various shock widths. Each data-point corresponds to a stable $L_{lbox} = 400$ pc

the cut-off energies for the various cases discussed in this section. The maximum energy to which a particle can be accelerated depends on the time the particle spends inside the acceleration zone or more specifically the number of shock crossings it has undergone. Since a distribution of scattering centres alters the escape probability, it also alters the maximum energy to which particles can be accelerated. Therefore, Fig. 4.15 clearly alludes to the fact that a wider shock leads to a lower escape probability

4.6 Application to Experimental Results

This section briefly demonstrates how the results of this thesis can be applied to extract information from CR experimental data. However, this section will not be a full-fledged scientific analysis and instead, we will be performing more like a “back of the envelope” calculation with the sole purpose of demonstration.

The Pierre Auger Observatory is an international cosmic ray observatory spread over 3000 sq. Km in Argentina. The observatory consists of Surface Detectors (SDs) which are water tanks that track the Cherenkov light emitted by energetic particles upon interaction with water and Fluorescence Detectors which track the development of air-showers by observing ultraviolet light emitted by the particles high in the earth’s atmosphere.

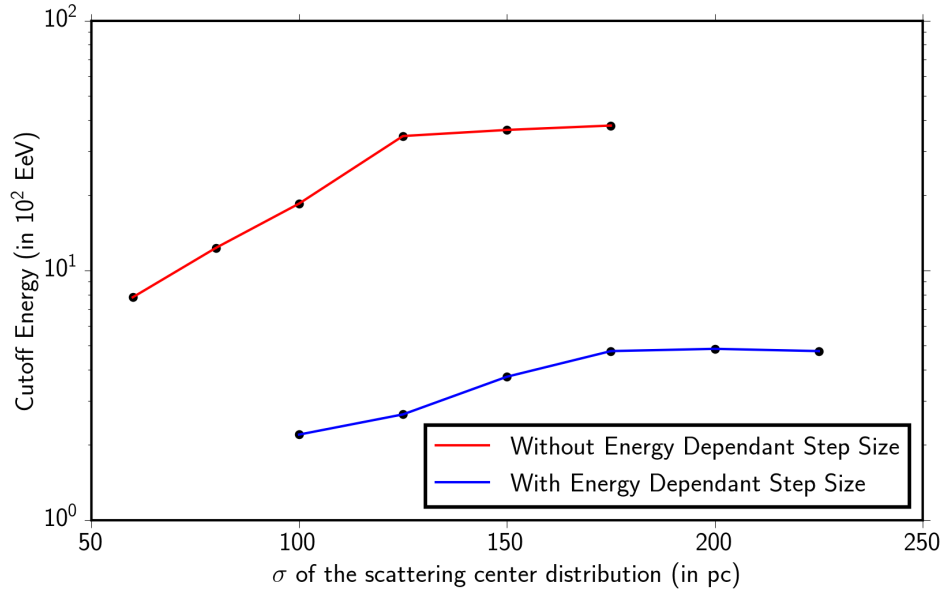


FIGURE 4.15: The spectral cut-off for various scattering shock widths , Each point corresponds to a stable downstream box-size

This hybrid nature of the observatory allows it to observe cosmic rays via two independent methods. Fig. 4.16 shows the spectrum of particles that is detected by Auger for different SD geometries.

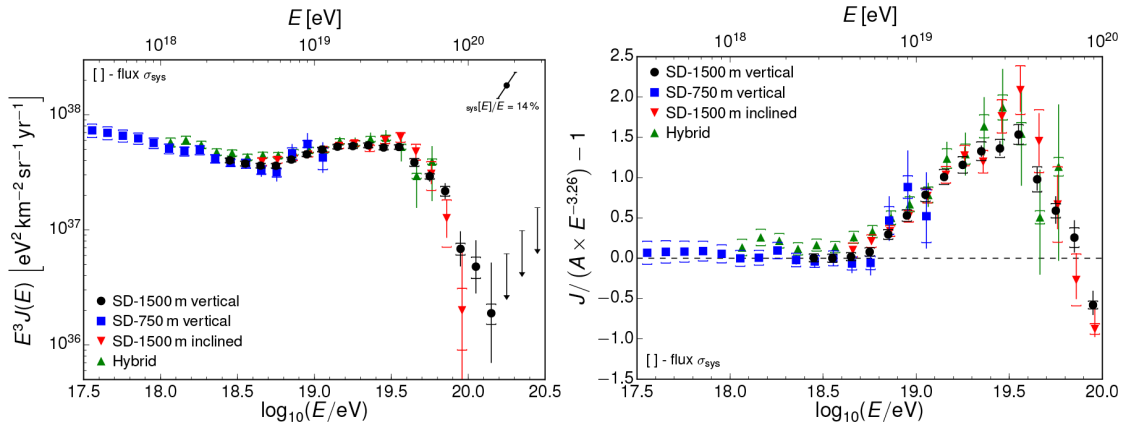


FIGURE 4.16: Left: energy spectra derived from Surface Detector(SD) and hybrid data recorded at the Pierre Auger Observatory. The error bars represent statistical uncertainties. The upper limits correspond to the 84% C.L. Right: fractional difference between the Auger spectra and a reference spectrum with an index of 3.26. Reproduced from Ref. [32]

In Fig. 4.16, there is clearly a cut-off in the spectrum around 10^2 EeV. Now, this is, of course, the spectrum detected on earth and there are propagation effects involved on top of source acceleration. However, for our purposes, we ignore these propagation effects. Now, if we assume that the acceleration occurs solely due to DSA by non-relativistic

shock-waves and simply compare this cut-off value with the energy dependent values in Fig. 4.15, we can conclude that such a shock-wave would have a shock width of the order of 100 pc. Now, this is with respect to an input MFP of 4 pc, a scale that has been chose by us. Let us now write the full expanded form of Eq. 4.3 from Ref. [31]

$$\lambda \simeq \frac{3}{(2\pi)^q(q-1)} \left[\frac{2}{(2-q)(4-q)} + \frac{q-1}{q-2} \left(\frac{V}{U} \right)^{q-2} \right] R_G^{q-2} \lambda_{\max}^{q-1} \left(\frac{B_0}{\delta B} \right)^2 \quad (4.4)$$

where the MFP $\lambda = 4$ pc, the turbulence index of the magnetic field $q = 5/3$, the particle velocity $V = c$, the shock velocity $U = 0.1c$, the wavelength of the largest possible Alfvén wave $\lambda_{\max} = 100$ pc, the magnetic irregularities ratio $B_0/\delta B = 10$ and the radius of gyration $R_G \sim 3.3 \times 10^{12} E_{\text{GeV}}/(ZB_{\mu\text{G}})$ [30]. Plugging in the value of the energy, we get a value of the magnetic field for the source to be of the order of 10 nG. From the Hillas plots shown in Fig. 4.17, it can be concluded the accelerator in this case could have been AGN jets or galaxy cluster shocks.

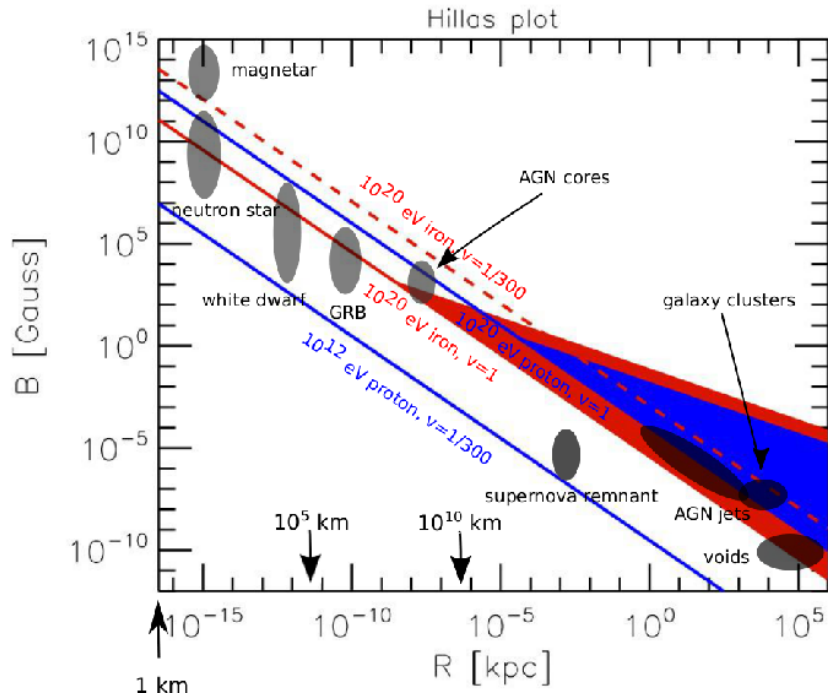


FIGURE 4.17: The “Hillas plot” represents astrophysical objects which are potential cosmic-ray accelerators on a two-dimensional diagram where on the horizontal direction the size linear extension R of the accelerator, and on the vertical direction the magnetic field strength B are plotted. Reproduced from Ref. [33].

Chapter 5

Conclusion

In this thesis, we demonstrated firmly that DSA can be included in CR Propa. Taking advantage of the easily extensible nature of CR Propa, we constructed our simulation framework by building our own Acceleration Module, Observers and using it in conjunction with the other preexisting modules as described in Chapter 3. After some initial calibration of parameters, we reproduced the standard DSA spectrum with a spectral index of -2.0 and also investigated limiting cases yielding softer spectra.

The relation of the spectrum with various geometrical parameters such as L_{lbox} and L_{rbox} were analyzed in Sec. 4.1. This has given us insight into exactly how the geometry of the acceleration region affects the particle spectrum. In order to ensure that our simulation agrees with previous theoretical predictions, we undertook detailed studies into the energy gain factor, escape probability and mean free path of scattering interactions in Secs. 4.2, 4.3. All our results show excellent agreement with theoretical predictions. We were also able to demonstrate that the simple treatment of DSA is no longer valid for (ultra) relativistic shocks and that results start showing significant divergence for shock velocities greater than $0.4c$

In Secs. 4.4, 4.5 we looked at two ways the simulation can be modified to include more detailed effects beyond “textbook” DSA. These two sections elucidated on how an energy dependent step length and a non-uniform distribution of scattering centres around the shock-front affect the index of the power law spectrum and the cutoff. Finally, in Sec. 4.6, we demonstrated how the results of this simulation may be used to infer information about experimental data.

By incorporating DSA within CR Propa, we have set up the base for a new way to tackle DSA via the microscopic route. As we have already demonstrated here, there are many ways to modify and extend our DSA module. As described in Chap. 3, CR Propa

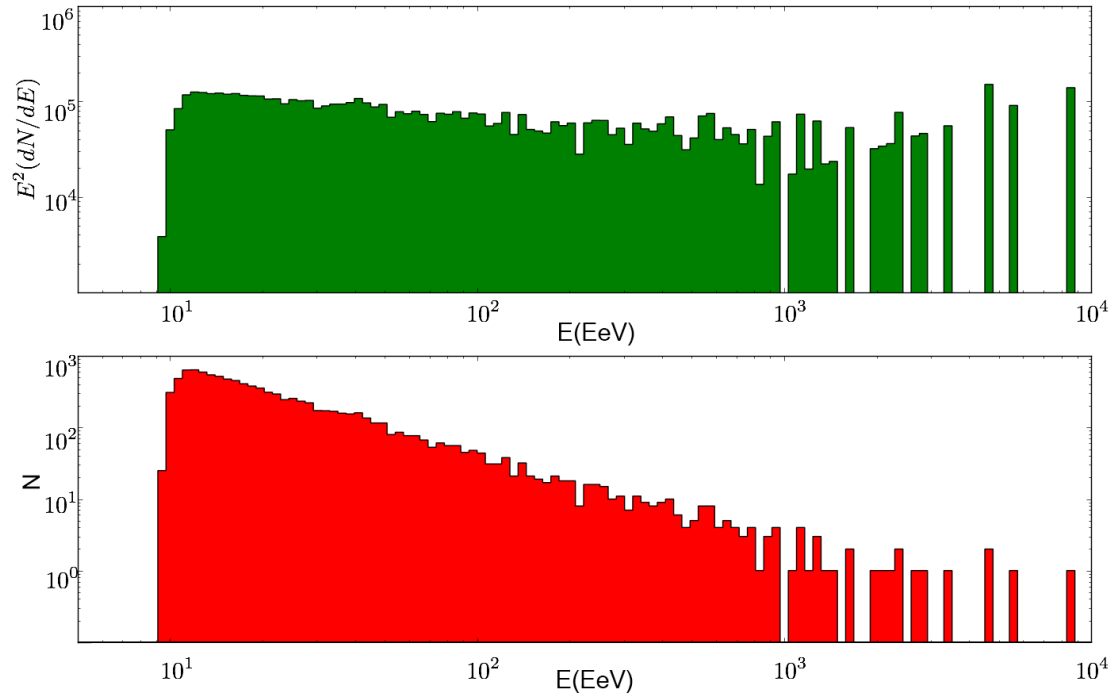
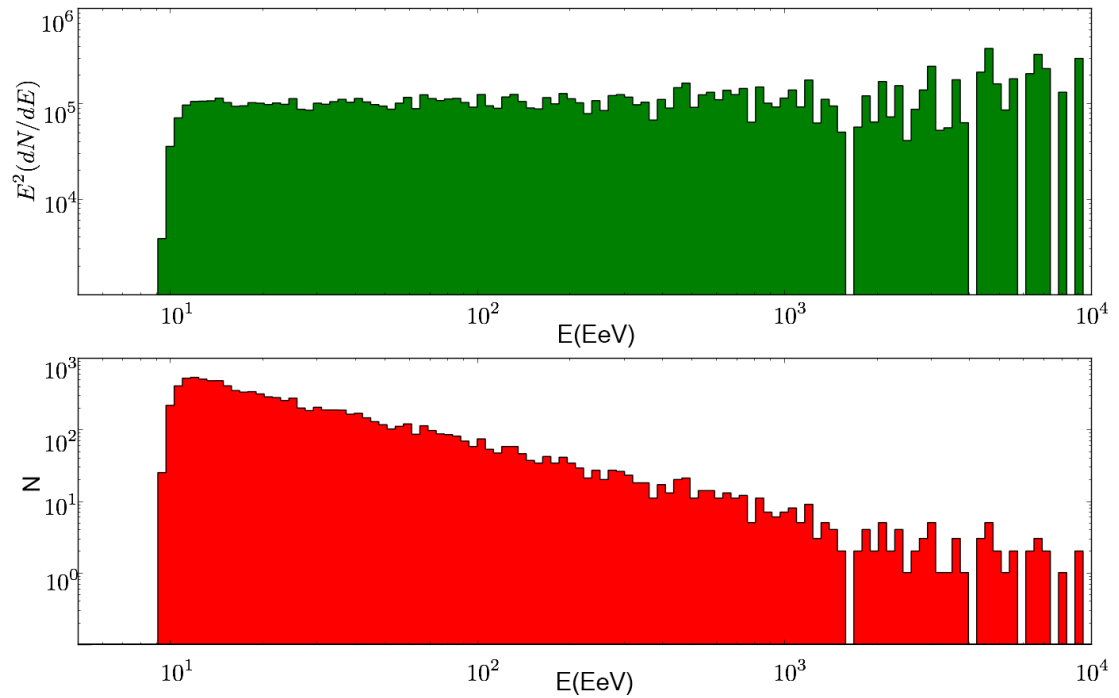
has in-built modules to simulate energy losses by interaction with background photons, expansion of the universe and create secondary nuclei, photons, neutrinos from various interactions and decays. By combining the Acceleration Module described herein with these pre-existing modules, it is possible to study scenarios which were earlier thought to be too involved analytically or too complicated to simulate. This thesis serves to be the first step towards such future studies.

Appendix A

Spectrum Images

This Appendix contains the spectra for all the different DSA scenarios studied in this thesis. Due to an inadequacy of space, only a few spectra for each scenario are included. However, care has been taken to ensure that all other spectra obtained are similar to the ones shown here. For all scenarios, at least two spectra are included, one for the “stable” value of L_{lbox} and another for an “unstable” value of the same. By unstable, we refer to the fact that if L_{lbox} is varied even slightly, the index of the power law changes substantially. This is not the case for the stable scenario, where a change in L_{lbox} produces almost a negligible change in the power law index.

The lower half of each figure represents the energy spectrum i.e. the number of particles as a function of the energy, while the upper half is the differential energy spectrum i.e. $\frac{\text{number of particles}}{\text{bin-width}} * (\text{Energy})^2$ as a function of the energy. In the differential energy spectrum, a horizontal line corresponds to the canonical -2.0 spectrum.

Standard DSAFIGURE A.1: Spectrum for standard DSA with $L_{lbox} = 80 pc$ [Unstable]FIGURE A.2: Spectrum for standard DSA with $L_{lbox} = 500 pc$ [Stable]

DSA with Energy Dependant Scattering Rate

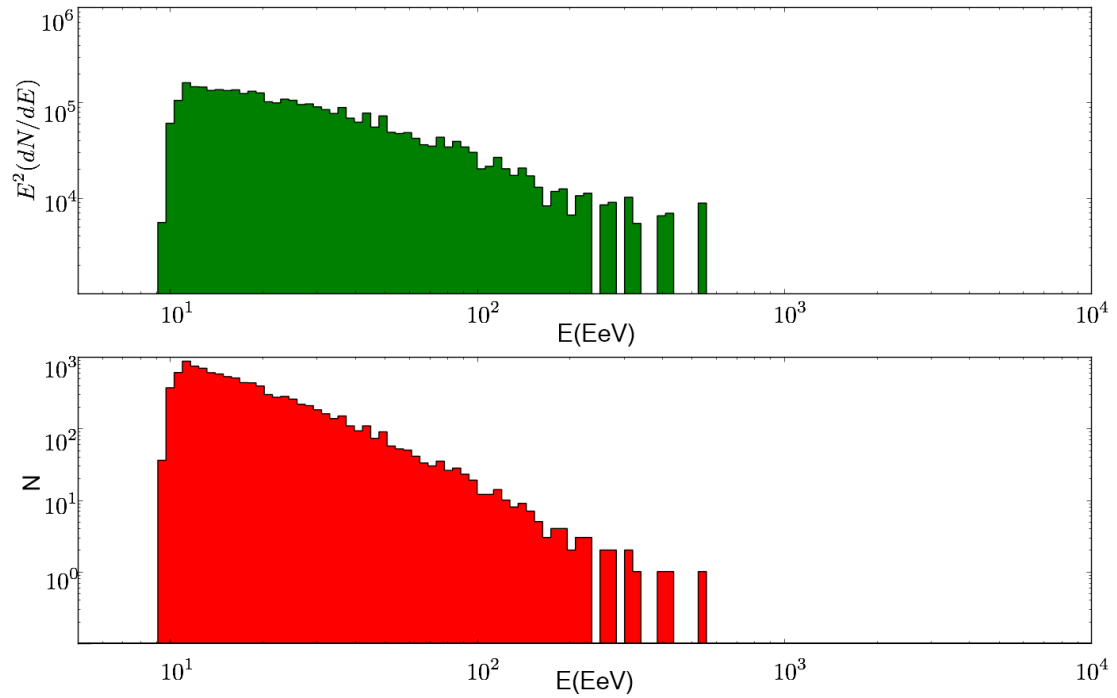


FIGURE A.3: Spectrum for DSA with energy dependant scattering rate $L_{lbox} = 120 pc$ [Unstable]

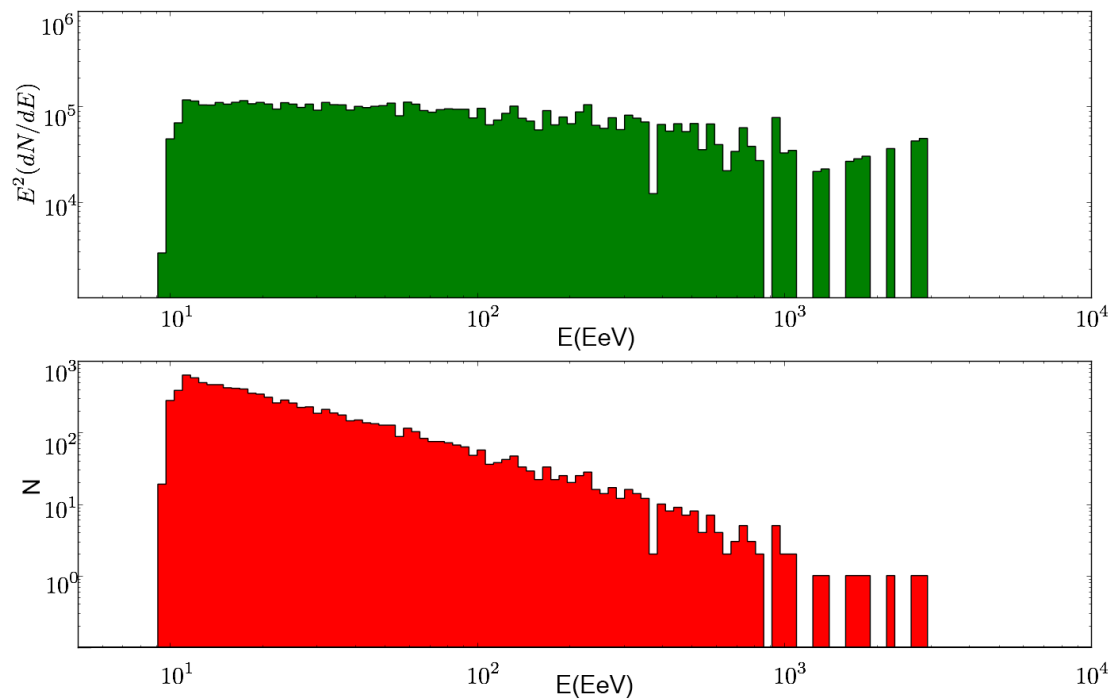
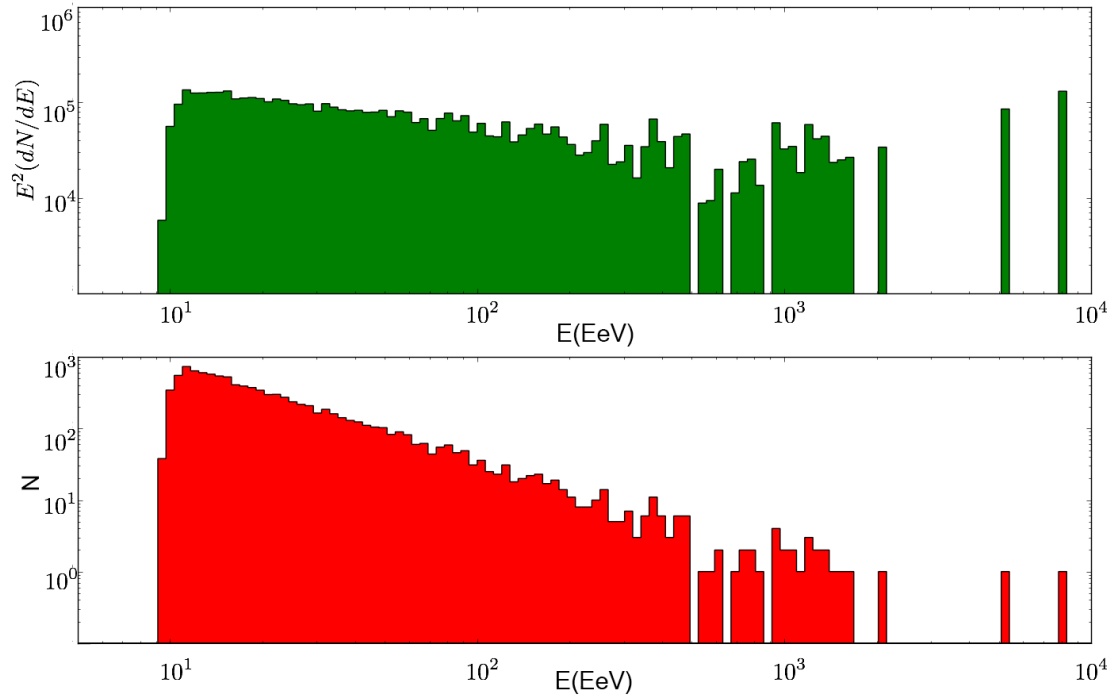
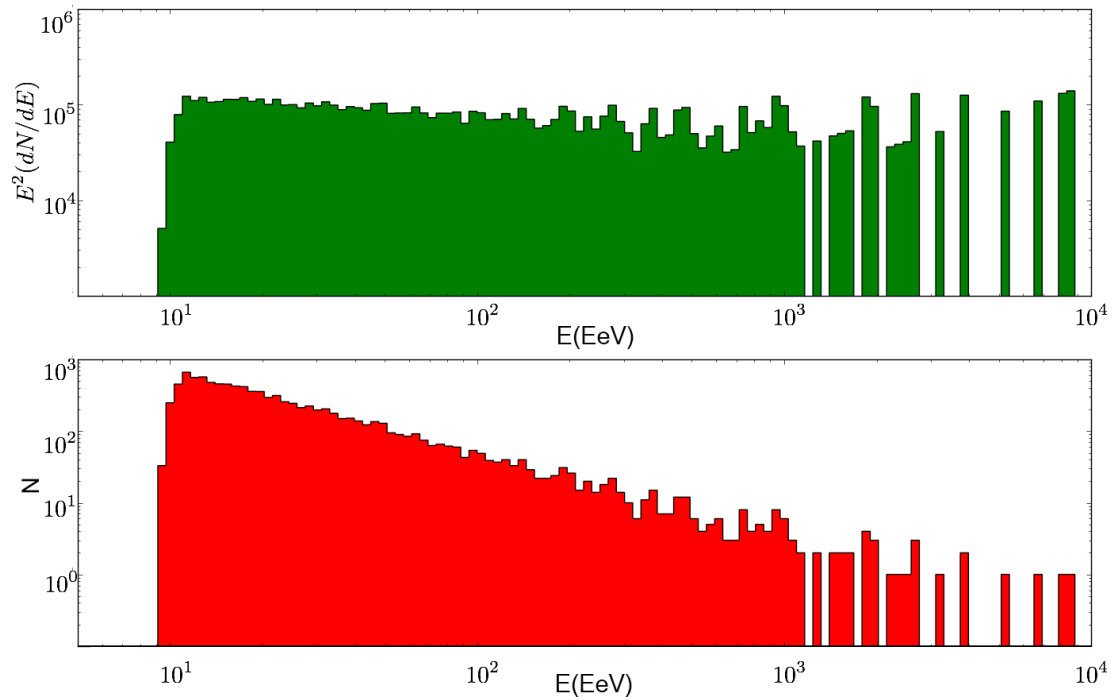


FIGURE A.4: Spectrum for DSA with energy dependant scattering rate $L_{lbox} = 500 pc$ [Stable]

DSA with Variable Scattering Centre Density

$$\sigma = 80 pc$$

FIGURE A.5: Spectrum for DSA with a shock width of $80 pc$ $L_{box} = 80 pc$ [Unstable]FIGURE A.6: Spectrum for DSA with a shock width of $80 pc$ $L_{box} = 400 pc$ [Stable]

$\sigma = 175 pc$

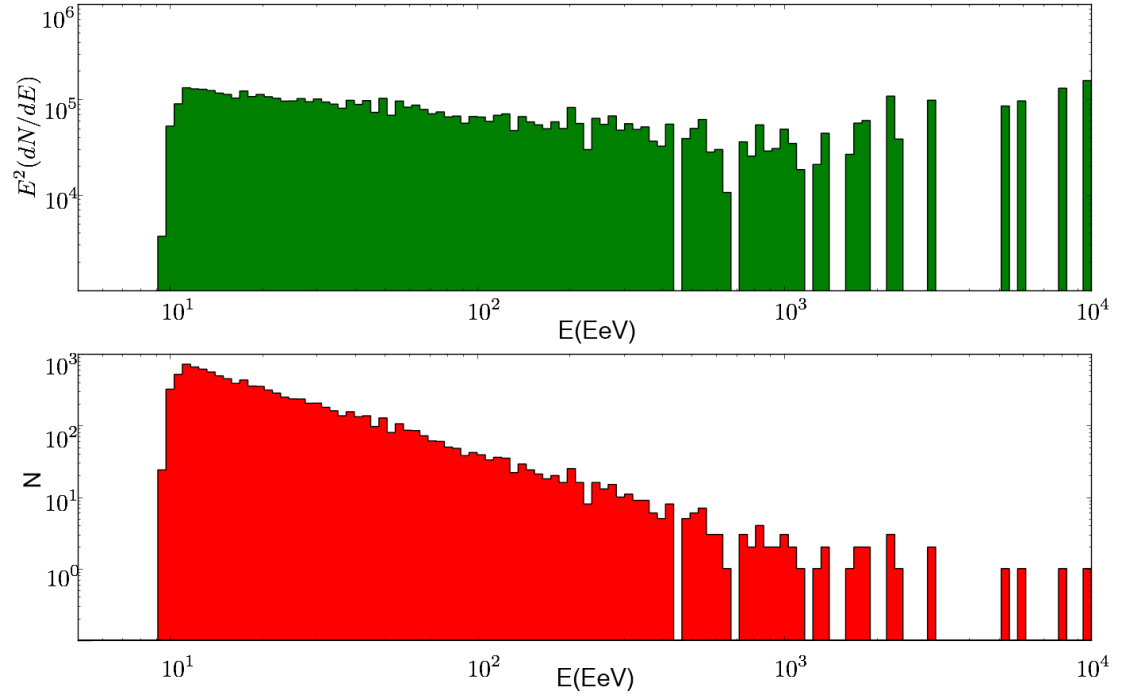


FIGURE A.7: Spectrum for DSA with a shock width of $175 pc$ $L_{box} = 80 pc$ [Unstable]

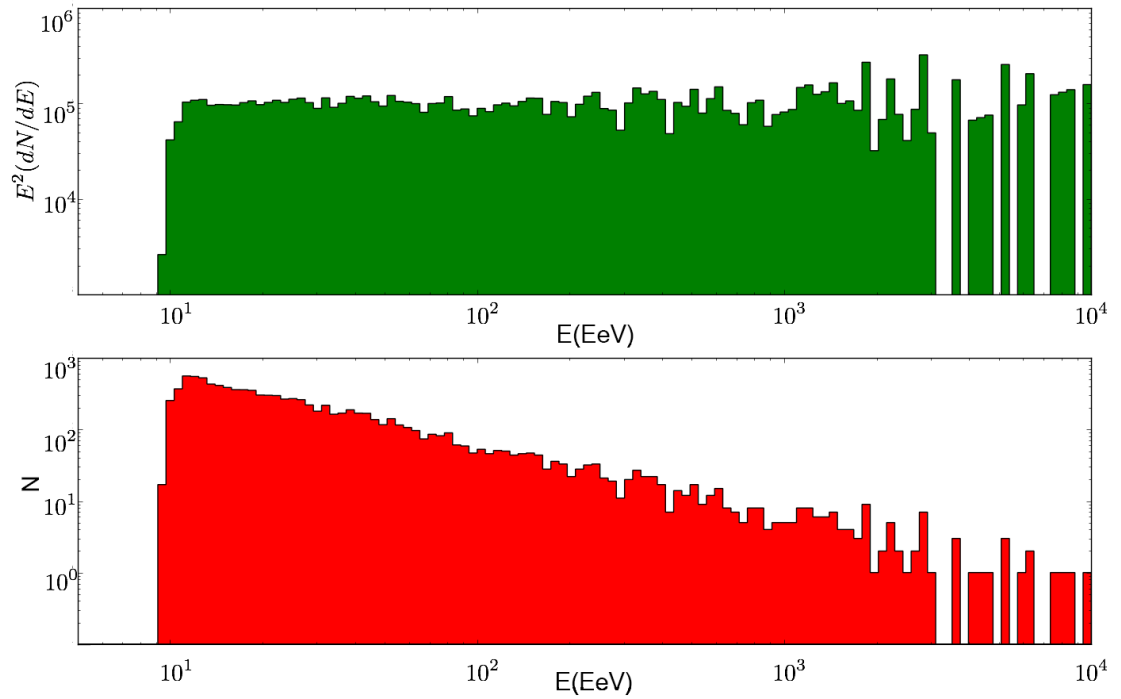


FIGURE A.8: Spectrum for DSA with a shock width of $175 pc$ $L_{box} = 400 pc$ [Stable]

DSA with Energy dependent Rate & Shock-width

$$\sigma = 125 pc$$

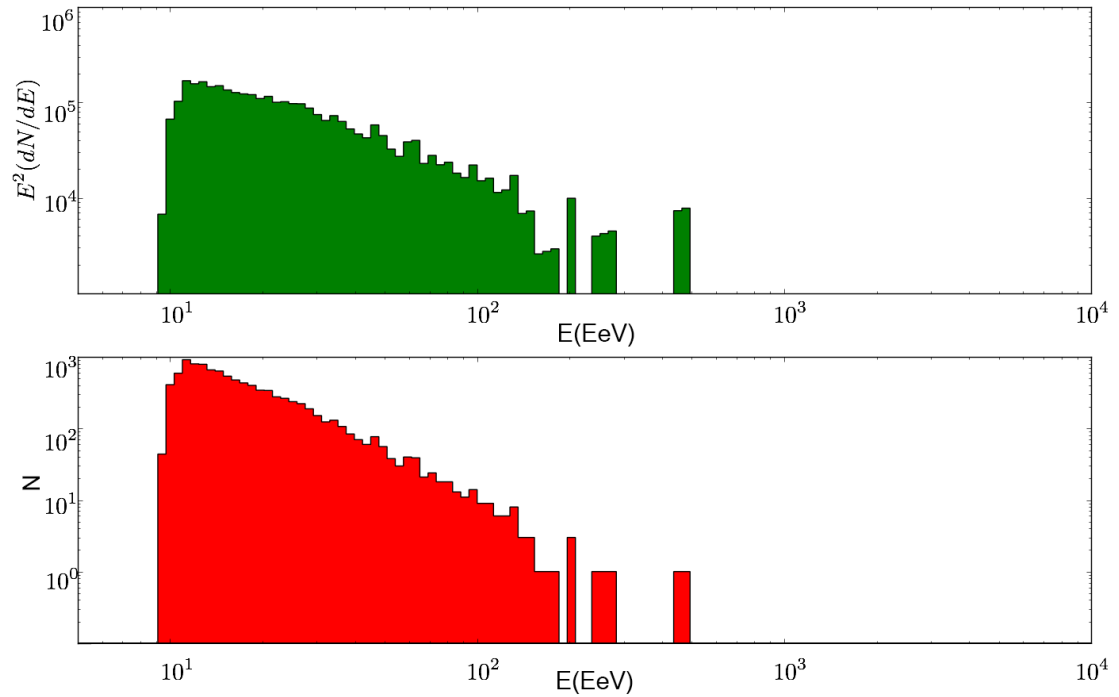


FIGURE A.9: Spectrum for DSA with energy dependant scattering rate and a shock width of $125 pc$ $L_{lbox} = 120 pc$ [Unstable]

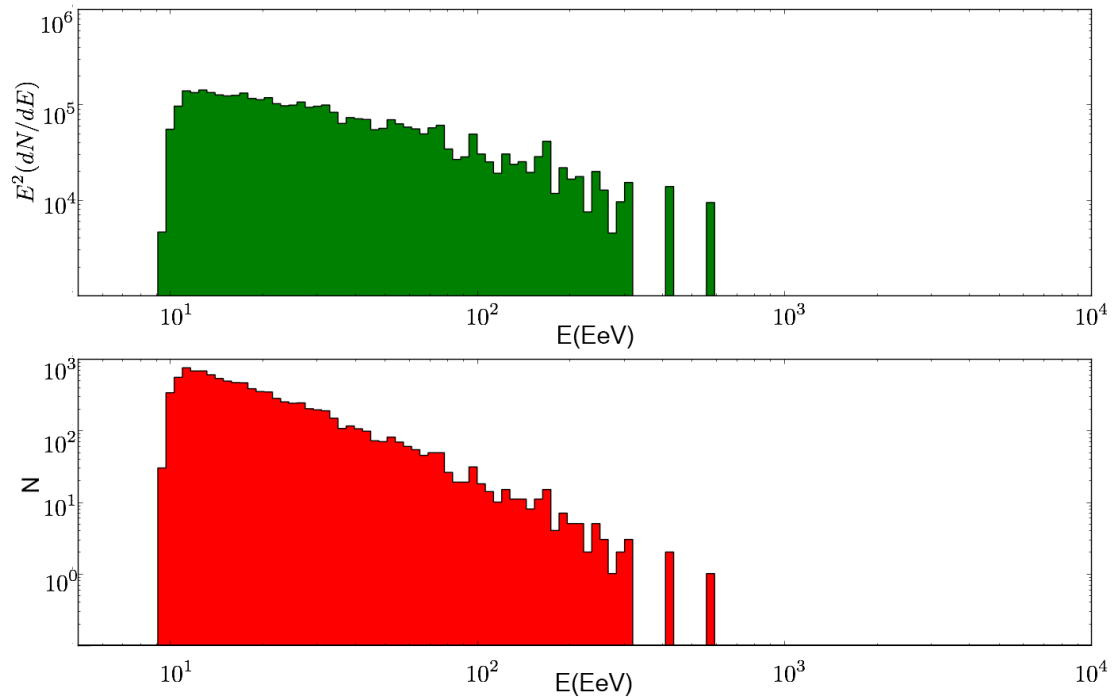


FIGURE A.10: Spectrum for DSA with energy dependant scattering rate and a shock width of $125 pc$ $L_{lbox} = 400 pc$ [Stable]

$\sigma = 225 pc$

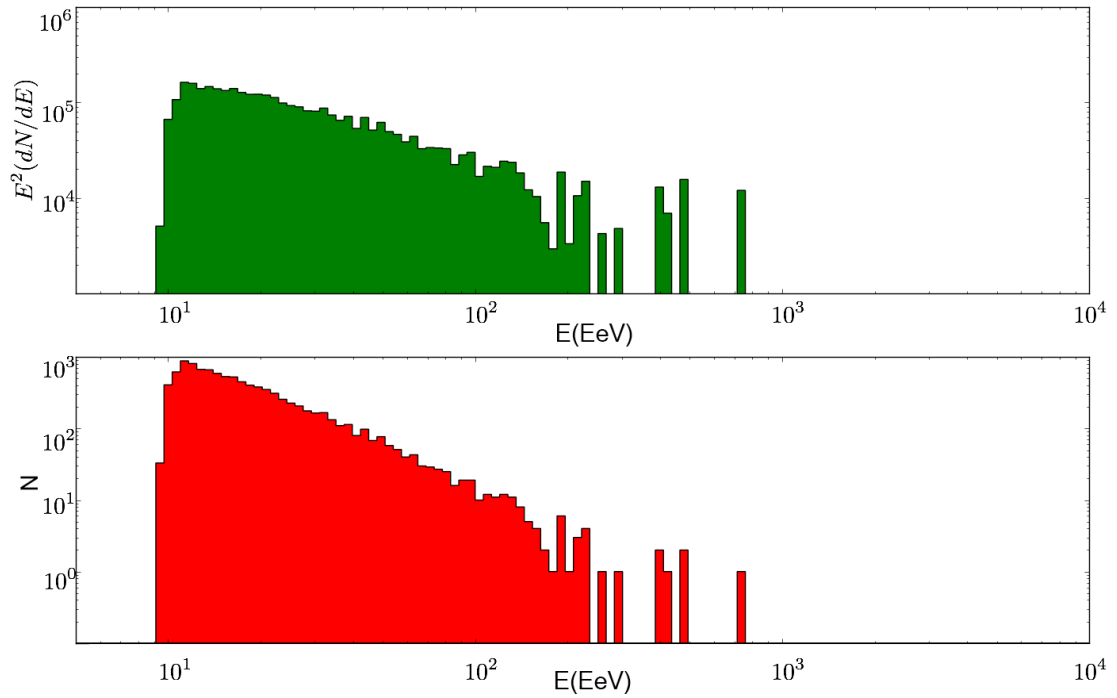


FIGURE A.11: Spectrum for DSA with energy dependant scattering rate and a shock width of $225 pc$ $L_{box} = 120 pc$ [Unstable]

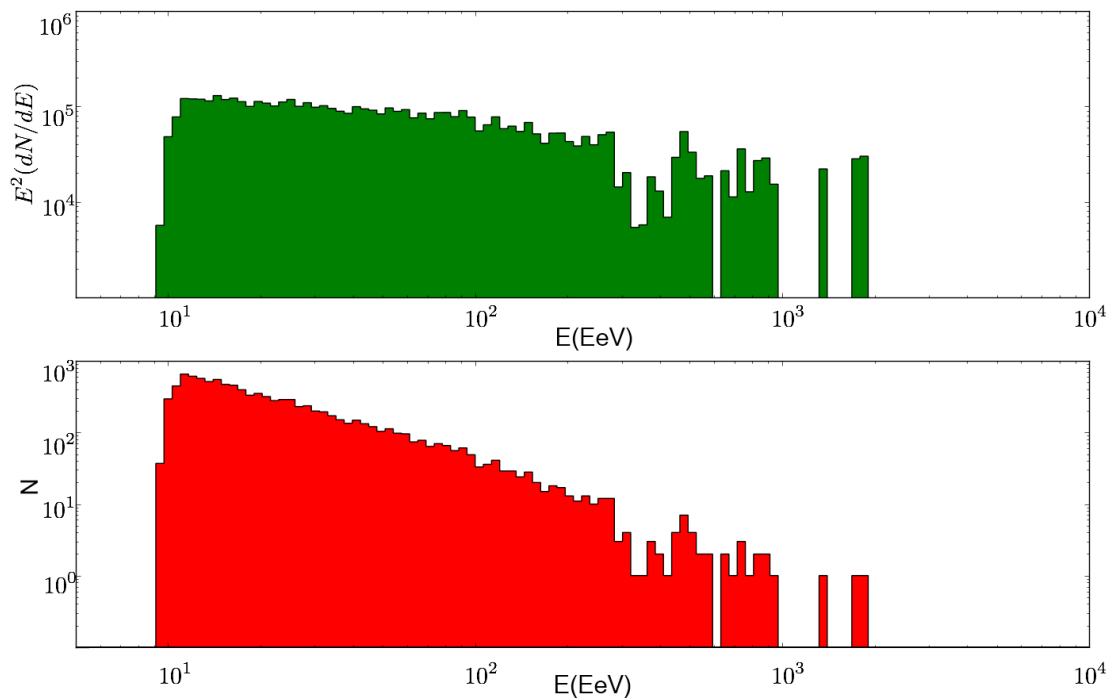


FIGURE A.12: Spectrum for DSA with energy dependant scattering rate and a shock width of $225 pc$ $L_{box} = 400 pc$ [Stable]

Bibliography

- [1] J. Abraham et al. Measurement of the energy spectrum of cosmic rays above 10^{18} eV using the Pierre Auger Observatory. *Physics Letters B*, **685** (4–5) 239 – 246, 2010. [[astro-ph.HE/1002.1975](#)].
- [2] K. Kotera and A. V. Olinto. The Astrophysics of Ultrahigh-Energy Cosmic Rays. *Annual Review of Astronomy and Astrophysics*, **49** (1) 119–153, 2011. [[astro-ph.HE/1101.4256](#)].
- [3] A. Aab et al. Depth of maximum of air-shower profiles at the Pierre Auger Observatory. II. Composition implications. *Physical Review D*, **90** 122006, 2014. [[astro-ph.HE/1409.5083](#)].
- [4] Y. Tsunesada et al. Highlights from the Telescope Array. In *EPJ Web of Conferences*, volume 126, page 01001. EDP Sciences, 2016. [[astro-ph.HE/1111.2507](#)].
- [5] R. A. Batista et al. CRPropa 3—a public astrophysical simulation framework for propagating extraterrestrial ultra-high energy particles. *Journal of Cosmology and Astroparticle Physics*, **2016** (05) 038–038, 2016. [[astro-ph.IM/1603.07142](#)].
- [6] A. M. Hillas. Cosmic Rays: Recent Progress and some Current Questions. *arXiv:astro-ph/0607109v2*, 2006.
- [7] R. Blandford, P. Simeon and Y. Yuan. Cosmic Ray Origins: An Introduction. *Nuclear Physics B - Proceedings Supplements*, **256** 9 – 22, 2014. [[astro-ph.HE/1409.2589](#)].
- [8] D. Allard, E. Parizot and A. Olinto. On the transition from galactic to extragalactic cosmic-rays: Spectral and composition features from two opposite scenarios. *Astroparticle Physics*, **27** (1) 61 – 75, 2007. [[astro-ph/0512345](#)].
- [9] E. G. Berezhko. Composition of Cosmic Rays Accelerated in Active Galactic Nuclei. *The Astrophysical Journal Letters*, **698** (2) L138, 2009. [[astro-ph.HE/0905.4785](#)].

- [10] P. Baerwald, M. Bustamante and W. Winter. Are gamma-ray bursts the sources of ultra-high energy cosmic rays? *Astroparticle Physics*, **62** 66 – 91, 2015. [astro-ph.HE/1401.1820].
- [11] K. Fang, K. Kotera and A. V. Olinto. Newly born pulsars as sources of ultrahigh energy cosmic rays. *The Astrophysical Journal*, **750** (2) 118, 2012. [astro-ph.HE/1201.5197].
- [12] H. Kang, D. Ryu and T. W. Jones. Cluster Accretion Shocks as Possible Acceleration Sites for Ultra-High-Energy Protons below the Greisen Cutoff. *The Astrophysical Journal*, **456** 422, 1996. [astro-ph/9507113].
- [13] A. R. Bell. The acceleration of cosmic rays in shock fronts. I. *Monthly Notices of the Royal Astronomical Society*, **182** 147–156, 1978.
- [14] R. D. Blandford and J. P. Ostriker. Particle acceleration by astrophysical shocks. *The Astrophysical Journal Letters*, **221** L29–L32, 1978.
- [15] E. Fermi. On the Origin of the Cosmic Radiation. *Physical Review*, **75** 1169–1174, 1949.
- [16] A. Achterberg et al. Particle acceleration by ultrarelativistic shocks: theory and simulations. *Monthly Notices of the Royal Astronomical Society*, **328** (2) 393–408, 2001. [astro-ph/0107530].
- [17] K. A. Eriksen et al. Evidence for particle acceleration to the knee of the cosmic ray spectrum in Tycho’s supernova remnant. *The Astrophysical Journal Letters*, **728** (2) L28, 2011. [astro-ph.HE/1101.1454].
- [18] M. Ackermann et al. Detection of the characteristic pion-decay signature in supernova remnants. *Science*, **339** (6121) 807–811, 2013. [astro-ph.HE/1302.3307].
- [19] A. Giuliani et al. Neutral pion emission from accelerated protons in the supernova remnant W44. *The Astrophysical Journal Letters*, **742** (2) L30, 2011. [astro-ph.HE/1111.4868].
- [20] M. Aartsen et al. Observation of High-Energy Astrophysical Neutrinos in Three Years of IceCube Data. *Physical Review Letters*, **113** 101101, 2014. [astro-ph.HE/1405.5303].
- [21] M. Aartsen et al. Search for correlations between the arrival directions of IceCube neutrino events and ultrahigh-energy cosmic rays detected by the Pierre Auger Observatory and the Telescope Array. *Journal of Cosmology and Astroparticle Physics*, **2016** (01) 037, 2016. [astro-ph.HE/1511.09408].

- [22] A. Bykov et al. Ultrahard spectra of PeV neutrinos from supernovae in compact star clusters. *Monthly Notices of the Royal Astronomical Society*, **453** (1) 113, 2015. [astro-ph.HE/1507.04018].
- [23] C. Ko and J. Jokipii. A numerical study of diffusive shock acceleration of cosmic rays in supernova shocks. In *Proceedings of the International Cosmic Ray Conference*, volume 3. 1985.
- [24] H. Kang and T. Jones. Numerical studies of diffusive shock acceleration at spherical shocks. *Astroparticle Physics*, **25** (4) 246 – 258, 2006. [astro-ph./0603223].
- [25] B. Achterberg. Cosmic Accelerators, 2008. Prepared for IAC 2008.
- [26] M. Longair. *High Energy Astrophysics*. Cambridge University Press, 2011.
- [27] D. G. Wentzel. Cosmic-ray propagation in the galaxy: Collective effects. *Annual Review of Astronomy and Astrophysics*, **12** (1) 71–96, 1974.
- [28] C. J. Cesarsky. Cosmic-ray confinement in the galaxy. *Annual Review of Astronomy and Astrophysics*, **18** (1) 289–319, 1980.
- [29] J. Beijers. Introduction to Plasma Physics, 2006. University of Groningen Lecture Notes.
- [30] J. Scalo and B. G. Elmegreen. Interstellar turbulence II: Implications and effects. *Annual Review of Astronomy and Astrophysics*, **42** 275–316, 2004. [astro-ph./0404452].
- [31] R. Schlickeiser. Cosmic-ray transport and acceleration. II. Cosmic rays in moving cold media with application to diffusive shock wave acceleration. *The Astrophysical Journal*, **336** 264, 1989.
- [32] A. Aab et al. The Pierre Auger Observatory: Contributions to the 34th International Cosmic Ray Conference (ICRC 2015). *arXiv:1509.03732*, 2015.
- [33] G. Sigl. High Energy Neutrinos and Cosmic Rays. *Proceedings of the International School of Physics Fermi*, **182** 145–184, 2012. [astro-ph.HE/1202.0466].